ACS Catalysis

pubs.acs.org/acscatalysis Research Article

Breaking the Code of Active Sites in CO_2-Assisted Propane Dehydrogenation over Mg(Fe,Al)O_x

Lennert A. D'ooghe, Servaas Lips, Soumya Kumar Das, Lukas C. Buelens, Alessandro Longo, Hilde Poelman, Kevin M. Van Geem, and Vladimir V. Galvita*

Cite This: ACS Catal. 2026, 16, 3999–4016 Read Online

ACCESS | Metrics & More | Article Recommendations | Supporting Information

ABSTRACT: Unlocking the full potential of CO_2 as a mild oxidant in propane dehydrogenation (CO_2–PDH) hinges on mastering the redox chemistry of metal oxide catalysts, that are suited to activate C–H bonds, while mitigating deactivation. This work explores a Mg(5 wt % Fe,Al)O_x catalyst, synthesized as layered double hydroxide. The ensuing stabilization of oxidized iron within Mg(Fe,Al)O_x yields intricate redox dynamics during CO_2–PDH. Fe-normalized time yields between 2.0 and 5.6 $mmol_{C3H6} \cdot mol_{Fe}^{-1} \cdot s^{-1}$ place Mg(Fe,Al)O_x among the most efficient Fe-based systems reported to date. The catalyst withstands CO_2–PDH – O_2 regeneration cycles without loss of initial activity. While gradual deactivation occurs across 20 h time-on-stream, the propylene selectivity stabilizes at 78.9%, underscoring the potential for prolonged operation. The intricate redox dynamics were investigated using time-resolved XAS and XRD with modulation-excitation. This approach enabled the decoding of two distinct CO_2–PDH pathways. First, iron reversibly cycles between Fe^{3+} in a surface $MgFe_2O_4$ phase and dispersed Fe^{2+} species, via $Fe^{3+} \rightleftharpoons Fe^{3+/2+} \rightleftharpoons Fe^{2+}$ transitions. This Mars-van Krevelen pathway enables carbon removal, but can also overoxidize hydrocarbons. In a parallel Langmuir–Hinshelwood pathway, these Fe^{2+} species, stabilized by an MgO-like environment in a likely distorted coordination, serve as highly selective sites for C–H bond activation. Although only ~ 1% of Fe participates, it governs the catalytic performance. In contrast, irreversible $Fe^{3+} \rightleftharpoons Fe^{3+/2+} \rightleftharpoons Fe^{2+}$ transitions lead to $MgFe_2O_4$ depletion and aggregation of FeO_x, the latter promoting carbon formation. These structure–activity relationships break the long-standing code of active site identity and dynamics in Fe-based CO_2–PDH catalysts, highlighting both Fe dispersion and the Fe^{3+}/Fe^{2+} speciation as critical levers for optimizing performance.

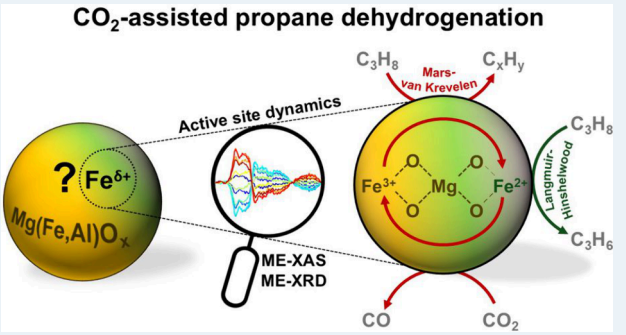

KEYWORDS: *CO_2-assisted propane dehydrogenation, Layered double hydroxide, Iron oxide, Redox properties, Modulation-excitation, X-ray spectroscopy, X-ray diffraction*

1. INTRODUCTION

Propylene, the second most important olefin after ethylene, is a crucial building block in the chemical industry.[1] Approximately 15–20% of the global propylene output stems from propane dehydrogenation (PDH, eq 1).[2] Unlike the nonselective steam cracking, PDH enables on-purpose propylene production.[3] A major challenge of the PDH process is its endothermic and equilibrium-limited nature, which requires temperatures above 800 K to achieve sufficiently high per-pass propane conversions.[4,5] Such temperatures, however, also promote carbon formation, thereby accelerating catalyst deactivation. Consequently, industrial PDH process technology requires frequent catalyst regeneration cycles, resulting in additional energy demand, process downtime, and ultimately, permanent catalyst deactivation.[4−9]

In the past two decades, oxidative PDH strategies have gained interest as a means to address these challenges.[3,10−13] Introducing an oxidant into the PDH process enables H_2 oxidation, causing an equilibrium shift toward propylene, while oxidizing carbon deposits and preserving the accessibility of active sites for propane adsorption. Mild oxidants are preferred over O_2 to avoid hydrocarbon overoxidation and excessive exothermicity. Among the mild oxidants, the use of CO_2 ("*CO_2–PDH*" or "*CO_2-assisted PDH*") has received notable interest[10,12] and is additionally incentivized as a strategy to mitigate climate change.[14] In CO_2–PDH, CO_2 can participate either via a two-step mechanism, in which dehydrogenation (eq 1) is followed by the reverse water–gas shift reaction (RWGS, eq 2), or via a one-step interaction with propane (eq

Received: December 21, 2025
Revised: January 26, 2026
Accepted: January 29, 2026
Published: February 6, 2026

3).[2] Additionally, CO_2 can oxidize carbon deposits via the reverse Boudouard reaction (eq 4).

$$C_3H_8 \rightleftharpoons C_3H_6 + H_2 \left(\Delta H_{298} = +124 \frac{kJ}{mol}\right) \quad (1)$$

$$CO_2 + H_2 \rightleftharpoons H_2O + CO \left(\Delta H_{298} = +41 \frac{kJ}{mol}\right) \quad (2)$$

$$CO_2 + C_3H_8 \rightleftharpoons C_3H_6 + CO + H_2O \left(\Delta H_{298} = +164 \frac{kJ}{mol}\right) \quad (3)$$

$$C + CO_2 \rightleftharpoons 2CO \left(\Delta H_{298} = +172 \frac{kJ}{mol}\right) \quad (4)$$

Industrial nonoxidative PDH processes often employ Pt-based catalysts, with Pt−Sn as a notable example (e.g., Oleflex).[4−6,8,9] Extending the application of supported Pt−Sn and Pt−In catalysts from nonoxidative PDH toward CO_2−PDH was the focus of prior work.[15−17] While promising propylene yields were obtained, even relatively low CO_2:C_3H_8 molar feed ratios (1:8) led to disintegration of the alloyed nanoparticles through promoter oxidation.[17] As an alternative, research on CO_2−PDH using transition metal oxide catalysts has recently emerged. Compared to noble metal catalysts, these are more economical and potentially more stable in the presence of CO_2. Especially FeO_x has gained attention as affordable, nontoxic and environmentally benign catalyst material.[18] Moreover, its facile redox properties, proven activity for the RWGS reaction,[19−24] and ability to activate C−H bonds makes it a promising catalyst candidate.

Despite these promising properties, the performance of metal oxide catalysts and the associated knowledge on their structure−activity relationships are still insufficient to allow for the development of industrially viable CO_2−PDH processes.[3,25] For FeO_x catalysts specifically, the importance of maintaining dispersed $Fe^{\delta+}$ species ($2 \geq \delta \geq 3$) to preserve C−H bond selectivity has been reported for nonoxidative PDH.[26−28] In this context, Lewis acid−base catalytic mechanisms have been proposed within zeolite frameworks: Hu et al. demonstrated such a mechanism for isolated Fe^{2+} species,[27] while more recently, Alghannam and Bell reported similar behavior for isolated Fe^{3+} species.[28] While this knowledge provides a significant step forward in establishing structure−activity relationships, further details on active site properties remain a subject of debate. Moreover, the extension to CO_2−PDH introduces new unknowns to the structure−activity relationships reported for nonoxidative PDH. Not only does the presence of CO_2 modify the redox dynamics of Fe, but it also introduces additional pathways for H_2 and carbon oxidation, complicating the identification of the active sites. Previously proposed active Fe species range from carbides[29,30] to atomically dispersed three-coordinate Fe^{2+},[27] dispersed $Fe^{2+/3+}$,[31−34] and dispersed Fe^{3+} [28,35] Moreover, identification of an accompanying CO_2 activation pathway in the context of CO_2−PDH is not always reported.[18,36] Finally, the majority of these mechanistic propositions were made based on static catalyst characterization, while the dynamic behavior of these materials has rarely been considered. Although valuable, a static approach yields sample-averaged conclusions, which may overlook important mechanistic phenomena or the contributions of highly active minority species.[37−40]

To address the uncertainties associated with structure−activity relationships, time-resolved in situ studies are required on catalyst systems that stabilize dispersed $Fe^{\delta+}$ species under CO_2−PDH redox conditions. A promising pathway to stabilize such $Fe^{\delta+}$ species within a mixed oxide is provided by layered double hydroxides (LDHs),[41,42] the application of which is underexplored for CO_2−PDH. This work contributes to establishing structure−activity relationships for FeO_x catalysts in CO_2−PDH by employing an LDH synthesis route, by assessing (CO_2-)PDH performance, and by applying time-resolved in situ X-ray characterization techniques. An LDH-derived $Mg(Fe,Al)O_x$ catalyst with 5 wt % Fe was prepared, a nominal Fe loading based on material stability, performance stability and propylene iron-normalized time yield (Fe-TY, $mmol_{C3H6} \cdot mol_{Fe}^{-1} \cdot s^{-1}$) reported in literature (Table S1). Time-resolved quick X-ray absorption spectroscopy (QXAS) identified the local Fe environment during reactive and redox treatments, while in situ X-ray diffraction (XRD) provided detailed information on the concomitant overall material restructuring. Modulation-excitation (ME) approaches were used in both XRD and QXAS to differentiate between responsive (minority) species and spectator species. This differentiation provides an essential key to unlocking the mechanistic insight into the nature and evolution of active $Fe^{\delta+}$ sites for CO_2−PDH. Such knowledge can be relevant beyond CO_2−PDH, for other processes coupling CO_2 activation with alkane or alkene transformations, including dry reforming of methane[43,44] and the CO_2-assisted dehydrogenation of other light alkanes.[45,46]

2. MATERIALS AND METHODS

2.1. Catalyst Synthesis

A mixed oxide $Mg(Fe,Al)O_x$ catalyst was synthesized by calcining a layered double hydroxide (LDH) precursor, targeting 5 wt % Fe and an M^{3+}:(M^{2+}+M^{3+}) molar ratio of 1:8.

The LDH phase was prepared through a low supersaturation coprecipitation method,[41] using the following metal precursors: $Mg(NO_3)_2 \cdot 6H_2O$ (Sigma-Aldrich, ACS reagent, 99%), $Al(NO_3)_3 \cdot 9H_2O$ (Sigma-Aldrich, ACS reagent, ≥ 98%) and $Fe(NO_3)_3 \cdot 9H_2O$ (Sigma-Aldrich, ACS reagent, ≥ 98%). Further, Na_2CO_3 (Sigma-Aldrich, ACS reagent, ≥ 99.5%) was used as CO_3^{2-} anion source and NaOH (Sigma-Aldrich, reagent grade, ≥ 98% anhydrous) as precipitating agent.

A 200 mL aqueous cation solution with a total metal cation concentration of 0.25 M (Mg^{2+}, Al^{3+} and Fe^{3+}) was prepared by dissolving the appropriate precursor masses in purified water (i.e., 18.2 $M\Omega \cdot cm^{-1}$ resistivity at 298 K). Similarly, a 200 mL aqueous anion solution of 0.4 M CO_3^{2-} was prepared by dissolving the appropriate mass of Na_2CO_3 in purified water. These solutions were simultaneously added dropwise to a beaker containing 200 mL purified water at 333 K under vigorous stirring. The temperature was monitored using a stainless-steel temperature probe (IKA ETS D5) and maintained at a constant level. The pH of the synthesis mixture was maintained at 12 ± 0.1 through dropwise addition of an aqueous NaOH solution (2 M). The pH of the synthesis mixture was monitored continuously with an electrode (3-point calibrated VWR Phenomenal 221) and regularly verified with universal pH strips (Whatman). The final synthesis volume was 0.8 L. The coprecipitation took place over a 30 min timespan, after which the mixture was further aged for 24 h at room temperature (RT). Hereafter, the solution was filtered to obtain the precipitated LDH phase. To remove anions and Na^+ cations, the residue was washed with purified water until the filtrate reached neutral pH. Subsequently, the washed sample was dried for 24 h in air at 393 K. The dried material was then crushed into a fine powder and calcined for 5 h at

https://doi.org/10.1021/acscatal.5c09151
ACS Catal. 2026, 16, 3999−4016

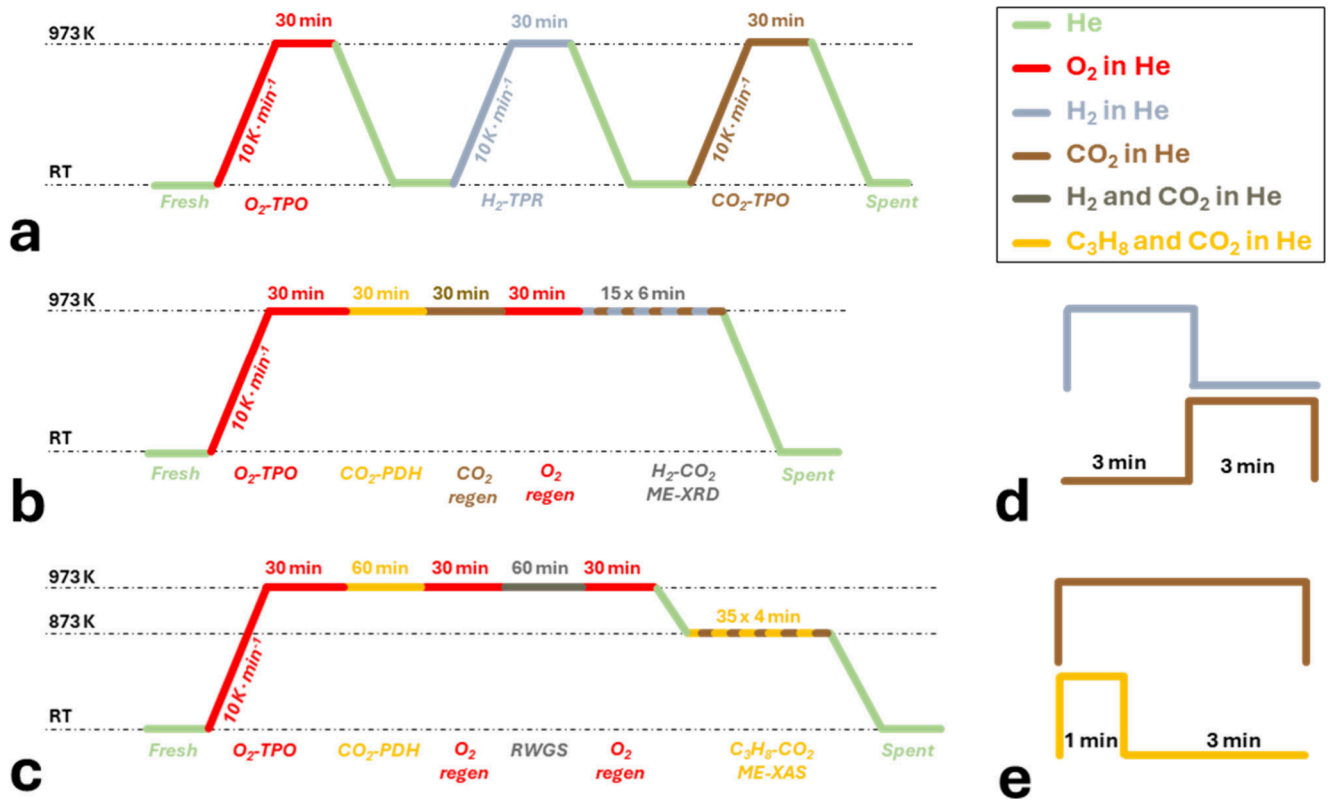

Figure 1. Experimental sequences used for the in situ X-ray characterization experiments. **a)** Sequence probing redox properties through O_2-TPO − H_2-TPR − CO_2-TPO. Used for XRD and QXAS. **b)** Sequence probing reactive properties, used for XRD. **c)** Sequence probing reactive properties, used for QXAS. **d)** Periodic H_2−CO_2 square wave modulations used for ME-XRD. **e)** Periodic C_3H_8−CO_2 rectangular wave modulations used for ME-XAS.

1073 K in a continuous air flow of 100 Nl·h^{-1}, employing a temperature ramp of 2 K·min^{-1}.

In addition to the LDH-derived Mg(Fe,Al)O_x, a physical mixture of Fe_2O_3 (Sigma-Aldrich, 99.999%) and MgO (Sigma-Aldrich, ≥ 99.99%) was made as reference sample, employing the same molar Fe:Mg ratio as in the Mg(Fe,Al)O_x catalyst. The physical mixture was prepared by repeatedly mixing and grinding it in an agate mortar to achieve a homogeneous dispersion.

2.2. Synthesis Verification

2.2.1. N_2 Physisorption. The specific surface area was determined using the BET method, while porosity properties were calculated using the BJH method. A sample mass of 0.2 g (100−200 μm sieve fraction) was initially degassed at 523 K for 4 h under a continuous N_2 flow using a Micromeritics SmartPrep apparatus. Physisorption measurements were performed at 77 K with a Micromeritics Tristar II apparatus.

2.2.2. Electron Microscopy. SEM-EDX measurements were performed with a Jeol JSM 5400 equipped with an INCA x-act (Oxford Instruments) for Energy Dispersive X-ray (EDX) analysis at an acceleration voltage of 20 kV.

STEM images were acquired using a Jeol JEM-2200FS Cs corrected electron microscope, equipped with a Schottky-type field-emission gun (FEG) and a Jeol JED-2300D for EDX analysis. Measurements were performed at an acceleration voltage of 200 kV and a spot size of 1.5 nm. The catalyst sample was deposited onto a Ted Pella 200 mesh Cu grid with a holey carbon film.

2.2.3. XRD during Calcination. The calcination of the LDH precursor was monitored via in situ XRD to verify successful synthesis. Measurements were performed using a Bruker-AXS D8 Discover apparatus with linear Vantec detector, using Cu K_α radiation (wavelength: 1.54 Å).[47] Scans were taken in a 2θ range from 28° to 48° with 5 s collection time and a 2θ resolution of 0.1°. Fine catalyst powder was placed onto a silicon wafer, connected to a conductive heating strip. A sample mass of ∼ 0.02 g was used with flow rates of 160 N ml·min^{-1} N_2 and 40 N ml·min^{-1} O_2. Temperature control proceeded through a calibrated thermocouple. A temperature ramp of 5 K·min^{-1} was employed from RT to 1073 K.

2.3. X-ray Characterization under Redox and Reactive Conditions

In situ X-ray characterization for redox and reactive treatments was conducted at synchrotron facilities (Figure 1). These experiments comprised in situ X-ray diffraction (XRD) and quick X-ray absorption spectroscopy (QXAS). Both techniques use hard X-rays, allowing to probe the sample's structural evolution under reactive conditions. XRD provided information on the overall crystalline restructuring of the sample, while QXAS at the Fe K-edge provided complementary time-resolved information on the average local Fe environment, allowing the capture of transient phenomena. A modulation-excitation (ME) approach was used for both techniques to isolate the spectral contributions of responsive (minority) species from those of spectator species.[38,48−52]

2.3.1. Synchrotron XRD. *2.3.1.1. Measurement Setup.* In situ XRD measurements were performed at the ID20 beamline of the 6 GeV ESRF synchrotron (Grenoble, France).[53] A 200 mA beam from three U26 undulators was sent through a cryogenically cooled Si(111) crystal monochromator. The monochromatic beam was then focused to a spot size of approximately 40 μm x 80 μm (V x H) with a Kirkpatrick-Baez mirror system. The incident X-ray energy E_0 was set at 9686.9 eV (wavelength 1.2799 Å). Data were acquired with a Minipix TPX3 detector[54] in a 2θ range from 23.38° to 60.78° with 0.04° step size for full scans (corresponding to the range 28.26°-75.11° at Cu K_α wavelength). For ME-XRD, data was acquired in a 2θ range from 31.30° to 45.13° with 0.01° step size (corresponding to 38.68°-55.07° at Cu K_α wavelength).

Measurements were performed in a custom-made reactor cell with fine, undiluted catalyst powder pressed into a 0.5 mm-thick pellet.

https://doi.org/10.1021/acscatal.5c09151
ACS Catal. 2026, 16, 3999−4016

This pellet was placed on top of a resistive heating element, connected to a thermocouple for temperature control. An Al foil dome was then mounted over the pellet and heating element, see Figure S1.[43] This sealed off the pellet from the outside environment, while still allowing sufficient X-ray penetration through the Al dome. The reactor was connected to the cooling water circulation during high-temperature treatments. Flow control was achieved through a custom-built mobile gas rig equipped with calibrated mass flow controllers and pneumatic valves, connected to the reactor cell via Swagelok connections.

2.3.1.2. Experimental Plan. Two in situ sequences were applied, each starting with a fresh sample. A first sequence probed the redox properties of the material (Figure 1a). This consisted of an O_2-TPO pretreatment (4 N ml·min^{-1} O_2 and 16 N ml·min^{-1} He), a subsequent H_2-TPR (1 N ml·min^{-1} H_2 and 19 N ml·min^{-1} He) and a final CO_2-TPO (4 N ml·min^{-1} CO_2 and 16 N ml·min^{-1} He). Each time, a 10 K·min^{-1} ramp rate was applied toward a temperature set point (SP) of 973 K, followed by a 30 min dwell.

A second sequence probed the sample during reaction and regeneration steps (Figure 1b). The sequence again started with an O_2-TPO pretreatment (4 N ml·min^{-1} O_2 and 16 N ml·min^{-1} He) with 10 K·min^{-1} ramp rate toward an SP of 973 K, and a 30 min dwell. This was followed by an isothermal CO_2−PDH reaction (973 K SP, 4 N ml·min^{-1} C_3H_8, 4 N ml·min^{-1} CO_2 and 12 N ml·min^{-1} He, 30 min). After the CO_2−PDH reaction, the sample was regenerated isothermally (973 K SP) with CO_2 (soft regeneration, 30 min) and O_2 (harsh regeneration, 30 min). Finally, a square wave modulation-excitation XRD experiment (ME-XRD) was applied to probe the nonlocal response of the material (Figure 1d). This was performed over 15 periods of 6 min, each period consisting of 3 min H_2/He (1 N ml·min^{-1} H_2 and 19 N ml·min^{-1} He) followed by 3 min CO_2/He (4 N ml·min^{-1} CO_2 and 16 N ml·min^{-1} He). This ME protocol was chosen to balance the time resolution of the XRD setup with the requirements of successful data analysis via Phase-Sensitive Detection (PSD, see 2.3.3). The Nyquist criterion requires at least two sampling points per period, while a successful PSD analysis requires a sampling rate at least an order of magnitude faster than the imposed modulations.[38] The square waveform of 6 min allowed for the recording of 10 complete XRD patterns per period, while still maintaining sensitivity to minority responsive phases.

2.3.2. Synchrotron QXAS. *2.3.2.1. Measurement Setup.* In situ QXAS measurements at the Fe K-edge (7112 eV) were performed at the ROCK beamline of the 2.75 GeV SOLEIL synchrotron (Saint-Aubin, France), operating under a machine current of 450 mA in top-up hybrid mode. Spectra were recorded with a Si(111) monochromator oscillating at 2 Hz, using only the forward oscillation direction.[55,56] A mirror with B_4C coating was used for harmonics rejection. The resulting spot size on the sample was 500 μm x 230 μm (H x V). The X-ray intensities were recorded in transmission mode with N_2-filled ionization chambers. An Fe foil was used for the reference channel during measurements. Further, ex situ spectra were recorded for the metallic Fe foil itself, as well as for reference pellets of α-Fe_2O_3 (Sigma-Aldrich, 99.995%), γ-Fe_2O_3 (US Nano, 99.9%), Fe_3O_4 (Sigma-Aldrich, 99.99%), FeO (Sigma-Aldrich, 99.6%), spinel $MgFe_2O_4$, $Mg_2Fe_2O_5$ (SI, section S3), and Fe(acac)$_3$ (iron(III) acetylacetonate, Sigma-Aldrich, 97%).

Fine catalyst powder was diluted with boron nitride (mass ratio catalyst:BN of 1:2) and loaded between two quartz wool plugs in quartz capillaries (1.2 mm outer diameter, 10 μm wall thickness), yielding a catalyst bed length of 5 mm. The capillary was mounted in a frame equipped with Swagelok fittings and encased in a radiant furnace.[55] Temperature control proceeded through a calibrated thermocouple placed against the catalyst bed. Administration of gas flows proceeded through calibrated MFCs, always maintaining a total flow of 7.0 N ml·min^{-1}. With this configuration, the gas arrival time from the MFCs to the catalyst bed was around 25 s.[57] The capillary outlet gas composition was monitored with a Cirrus MKS mass spectrometer.

2.3.2.2. Experimental Plan. Two in situ treatment sequences were applied, each starting with a fresh sample. A first sequence (Figure 1a) probed the redox properties through an O_2-TPO (pretreatment, 1.4 N ml·min^{-1} O_2 and 5.6 N ml·min^{-1} He), a subsequent H_2-TPR (1.4 N ml·min^{-1} H_2 and 5.6 N ml·min^{-1} He) and a final CO_2-TPO (1.4 N ml·min^{-1} CO_2 and 5.6 N ml·min^{-1} He). Each time, a 10 K·min^{-1} ramp rate was applied toward a temperature 973 K, followed by a 30 min dwell.

A second sequence (Figure 1c) probed the sample during reactive conditions, starting with an O_2-TPO pretreatment (1.4 N ml·min^{-1} O_2 and 5.6 N ml·min^{-1} He) with 10 K·min^{-1} ramp rate toward 973 K. This was followed by an isothermal CO_2−PDH reaction (1.4 N ml·min^{-1} C_3H_8, 1.4 N ml·min^{-1} CO_2 and 4.2 N ml·min^{-1} He), and a 30 min O_2 regeneration (1.4 N ml·min^{-1} O_2 and 5.6 N ml·min^{-1} He). Then, the same sample was exposed to an isothermal RWGS reaction (973 K SP, 1.2 N ml·min^{-1} H_2, 1.4 N ml·min^{-1} CO_2 and 4.2 N ml·min^{-1} He) with a subsequent 30 min O_2 regeneration (1.4 N ml·min^{-1} O_2 and 5.6 N ml·min^{-1} He), before cooling down to 873 K in 7.0 N ml·min^{-1} He. At 873 K, rectangular wave modulation-excitation experiments were performed to probe the responsive Fe species in conditions emulating CO_2−PDH (Figure 1e). The gas concentrations were cycled in 35 periods of 4 min, each consisting of a 1 min C_3H_8 flow (1.4 N ml·min^{-1}), constant CO_2 flow (1.4 N ml·min^{-1}) and balanced He flow to maintain 7.0 N ml·min^{-1} as total flow. The high time-resolution of the QXAS setup enabled the use of a rectangular waveform instead of a square wave. The richer harmonic content of rectangular waveforms allows for a more thorough kinetic differentiation of Fe transformations.[58]

2.3.2.3. Data Analysis. The absorption spectra were extracted from the raw data using an energy grid with data points at 0.2 eV intervals between 7100 and 7250 eV, and at 2 eV intervals elsewhere. All spectra were energy-calibrated against the Fe foil, averaged and normalized using the Python GUI of Roudenko et al.[55] Averaging was performed per 10 spectra (5 s resolution), balancing the improvement in signal-to-noise ratio with the preservation of time resolution.

Analysis of the pre-edge proceeded in LARCH[59] by fitting of pseudo-Voigt peaks between 7108 and 7122 eV. First, the pre-edge feature was isolated from the main edge via subtraction of a background, consisting of a combined linear and Voigt function. For peak fitting, the amplitude and center of all pseudo-Voigt components were varied independently. The width and Lorentzian:Gaussian ratio of the pseudo-Voigt components were also varied but constrained to be equal for all components.[60] Analysis started with one pseudo-Voigt component. Additional components were added until no further improvements were found in the reduced χ^2 value, the Akaike information criterion value, and the uniformity of the residuals vs energy.

EXAFS analysis at the Fe K edge was performed on k^3-weighted data, with Fourier transformation in a k-range of 2.6 − 14.0 Å^{-1}, using a Kaiser-Bessel window with Δk of 1.5 Å^{-1}. Fitting of the EXAFS data was performed in the R-space magnitude and imaginary part, within the range 1.2 − 3.2 Å. The amplitude reduction factor S_0^2 was determined by fitting the first Fe−Fe shell of the measured reference Fe foil and then fixed at the obtained value of 0.83 for all fits. To respect the Nyquist criterion for EXAFS fitting, a minimal number of paths and parameters were used, such that the total number of fitted parameters was at most 2/3 of the maximum number of independent points.[61] The following crystal structures were used for fitting: α-Fe_2O_3, γ-Fe_2O_3, Fe_3O_4, FeO, Mg(Fe)O periclase, $MgFe_2O_4$ spinel, and α-Fe metal (SI, Table S4). Different fits were compared based on the R-factor and physical meaning of the fitted parameters. The R-factors of the reported fits are below 5%.

2.3.3. PSD Analysis in ME Experiments.

$$A(E, \varphi_k^{PSD}) = \frac{2}{\tau}\int_0^{\tau} A(E, t)\sin\left(k\frac{2\pi}{\tau}t + \varphi_k^{PSD}\right)dt \quad (5)$$

The results of the ME-XAS and ME-XRD experiments were analyzed with PSD using a lock-in amplifier analogon (eq 5).[48,49,62] This transforms the data from time to phase domain.

Herein, A represents the normalized absorption coefficient in QXAS or the normalized diffraction intensity in XRD. E represents the spectral position: energy in QXAS or the diffraction angle in XRD.

https://doi.org/10.1021/acscatal.5c09151
ACS Catal. 2026, 16, 3999−4016

Further, t represents the time, φ_k^{PSD} the demodulation phase angle at demodulation index k (integer), and τ the modulation time period. The use of eq 5 assumes the material's response oscillates around a quasi-steady state (QSS),[49] which was identified through Multivariate Curve Resolution-Alternating Least Squares (MCR-ALS) analysis using 2 principal components (PCs).[63,64] Results of the MCR-ALS analysis were evaluated based on the percentage lack of fit (LOF) relative to the experimental data, the percentage of data variance explained (R^2), and the standard deviation of residuals vs experimental data (σ), as defined by Jaumot et al.[63,64] All periods within the QSS regime were averaged into one period to improve the signal-to-noise ratio in PSD.[58,62] An additional verification of the QSS boundary consisted of performing PSD with a QSS regime containing additional periods (yielding different conclusions) and fewer periods (yielding the same conclusions).

2.4. Catalytic Activity Tests

2.4.1. Setup. CO_2−PDH activity tests were performed in a fixed bed quartz reactor tube with an internal diameter of 7.5 mm. The temperature was measured in the catalyst bed and externally at the reactor wall with K-type thermocouples. Calibrated Bronckhorst MFCs were used to control the gas feed. Changes in the gas feed were imposed as a step function using a four-way valve. For each reaction, the reactor was operated isothermally at a pressure of 121.3 kPa. The catalyst bed was diluted with inert α-Al_2O_3 in 100−200 μm sieved fraction, and kept in position by a quartz wool plug.

The absence of mass transfer limitations was assessed through the criteria of Carberry[65] and Weisz-Prater,[66] while the absence of heat transport limitations was assessed through the criteria of Mears[67] (SI, Table S2).

Prior to the activity measurements, an empty quartz reactor and a bed of α-Al_2O_3 and $MgAl_2O_4$ were tested under reaction conditions to confirm the absence of thermal contributions and setup effects to the measured activity.

2.4.2. Reverse Water−Gas Shift Reaction. The reverse water gas shift reaction (RWGS) serves as a model reaction with H_2 as reductant and CO_2 as soft oxidant, which can shift the dehydrogenation equilibrium by coupling eq 1 and eq 2. To assess such contribution in CO_2−PDH, the RWGS activity was studied separately. Reactions were performed isothermally at 873 K, 898 K, 923 K, 948 and 973 K. A catalyst mass (W_{cat}) of 0.200 g was mixed with 0.600 g inert α-Al_2O_3. An equimolar feed ratio of CO_2 and H_2 was used, diluted with Ar (30 N ml·min^{-1} CO_2, 30 N ml·min^{-1} H_2, 90 N ml·min^{-1} Ar). The resulting space time $W_{cat}{\cdot}F^0_{tot}{}^{-1}$ was 1.8 $kg_{cat}{\cdot}s{\cdot}mol^{-1}$.

2.4.3. CO_2−PDH Reactions. All CO_2−PDH reactions were performed at 873 K. A first series of experiments tested the samples at different CO_2:C_3H_8 feed ratios and at two space times: (1) $W_{cat}{\cdot}F^0_{tot}{}^{-1}$ = 1.8 $kg_{cat}{\cdot}s{\cdot}mol^{-1}$ with 0.200 g catalyst, 0.600 g inert α-Al_2O_3 and a total flow of 150 N ml·min^{-1}, and (2) $W_{cat}{\cdot}F^0_{tot}{}^{-1}$ = 10.8 $kg_{cat}{\cdot}s{\cdot}mol^{-1}$ with 0.800 g, 1.000 g inert α-Al_2O_3 and a total flow of 100 N ml·min^{-1}. A constant C_3H_8 partial pressure was maintained across experiments (26.7 vol %), while the CO_2:C_3H_8 molar feed ratios were varied: 1.0:1.0, 0.5:1.0 and 0.0:1.0. Reactions were performed for 20 min time on stream (TOS).

Additionally, the stability of the catalyst across CO_2−PDH − O_2 regeneration cycles was tested at $W_{cat}{\cdot}F^0_{tot}{}^{-1}$ = 10.8 $kg_{cat}{\cdot}s{\cdot}mol^{-1}$ and an equimolar CO_2:C_3H_8 feed ratio. The reaction was repeated 5 times, each time for 15 min TOS. In-between reactions, the catalyst was regenerated isothermally for 20 min in O_2 (20 N ml·min^{-1} O_2, 80 N ml·min^{-1} Ar).

Finally, a 20 h TOS stability test was performed at $W_{cat}{\cdot}F^0_{tot}{}^{-1}$ = 10.8 $kg_{cat}{\cdot}s{\cdot}mol^{-1}$ with an equimolar CO_2:C_3H_8 feed ratio.

2.4.4. Data Analysis. The reactor outlet was monitored with an online mass spectrometer (MS, Pfeiffer Omnistar) and gas chromatograph (GC, Thermo Scientific). MS signals were recorded at the following mass-to-charge ratios (m/z) in view of minimizing the overlap in mass fragments: m/z = 2 (H_2), m/z = 16 (CH_4), m/z = 18 (H_2O), m/z = 26 (C_2H_4), m/z = 28 (CO), m/z = 29 (C_3H_8), m/z = 32 (O_2), m/z = 40 (Ar), m/z = 41 (C_3H_6), m/z = 44 (CO_2). Calibration measurements were collected at RT after each reaction run to correct for overlapping MS fragments. GC data were recorded with a TCD using Ar as internal standard, allowing to quantify all but C_3 products. CH_4 was transferred to the FID detector on the same apparatus, allowing to quantify the entire hydrocarbon pool. The carbon balance (C_{error}) was assessed via eq 6 with deviations remaining below 5% for all reported results. The conversion of component i (X_i) was quantified via eq 7 and the selectivity from C_3H_8 toward C_3H_6 ($S_{C_3H_6}$) via eq 8.

$$C_{error} = \frac{\sum_i n_{C,i}(F_{i,in} - F_{i,out})}{\sum_i n_{C,i}F_{i,in}} \tag{6}$$

$$X_i = \frac{F_{i,in} - F_{i,out}}{F_{i,in}} \tag{7}$$

$$S_{C_3H_6} = \frac{F_{C_3H_6,out}}{F_{C_3H_8,in} - F_{C_3H_8,out}} \tag{8}$$

Here, F_i is the molar flow of component i and $n_{C,i}$ the carbon number of component i. Quantification of accumulated carbon after a reaction was performed by oxidizing the carbon isothermally in 20% O_2/Ar, and integrating the outlet flow of CO_2 (derived from the calibrated and defragmented MS signal at m/z = 44). Equilibrium conversions were calculated via Aspen Plus v14, using the corresponding experimental reaction conditions. For the calculations, the NRTL property method[68] and a Gibbs-free energy minimization method (RGibbs reactor block) were applied.

3. RESULTS

3.1. Synthesis Verification

The composition and porosity properties of the calcined Mg(Fe,Al)O_x catalyst are listed in Table 1. This indicates that a mesoporous material has been obtained, as confirmed by the type IV adsorption isotherm in Figure S2. The type H1 hysteresis loop points at a uniform range of mesopores, possibly combined with the presence of ink-bottle type pore shapes.[69] STEM-EDX (Figure 2) shows no clustering of Fe at the recorded scale, which was an important objective of the chosen synthesis route.

Table 1. Basic Characterization Results of the Mg(Fe,Al)O_x Sample after Calcination, with Average Values and Standard Deviations over Three Measurements[a]

			Composition (wt %)		
BET specific surface area ($m^2{\cdot}g_{cat}^{-1}$)	BJH average pore volume ($cm^3{\cdot}g_{cat}^{-1}$)	BJH average pore diameter (Å)	Mg	Al	Fe
97.6 ± 9.8	0.30 ± 0.01	126 ± 8	46.2 ± 0.3	4.3 ± 0.1	6.1 ± 0.2

[a]Composition is obtained from SEM-EDX.

The presence of an LDH phase during synthesis is confirmed by the XRD patterns of the material before and after calcination (Figure 3a). Before calcination, the pattern is dominated by contributions of LDH structures at 2θ positions of 11.2°, 22.2°, 34.2°, 38.3°, 44.9°, 59.8°, 61.1, 64.7° and 72.8°. The low-angle reflections at 11.2° and 22.2° correspond to (00l) planes and represent the interlayer spacing, while the higher-angle region displays broad, asymmetric nonbasal reflections and a characteristic intralayer doublet.[70,71] Hexagonal brugnatellite ($Mg_6Fe^{3+}(CO_3)(OH)_{13}{\cdot}4H_2O$, PDF card

https://doi.org/10.1021/acscatal.5c09151
ACS Catal. 2026, 16, 3999−4016

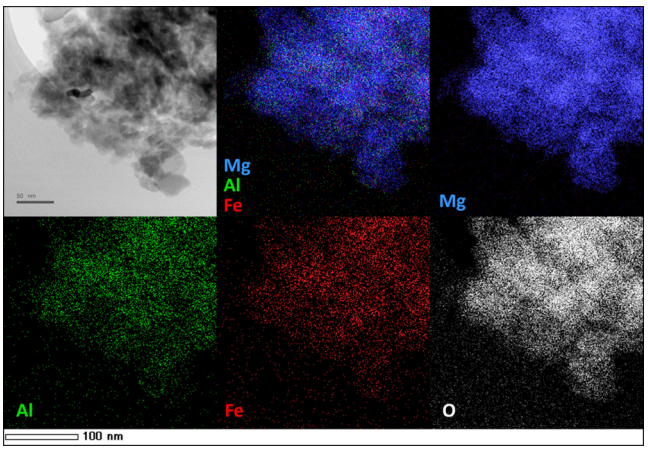

Figure 2. Bright-field STEM image of $Mg(Fe,Al)O_x$ after calcination, along with elemental EDX maps of the same region (K-edges). Data recorded at 200 000 kV, 500 000 x magnification and 1.5 nm spot size.

14−0365) and rhombohedral hydrotalcite ($Mg_6Al_2(CO_3)(OH)_{16}{\cdot}4H_2O$, PDF card 22−0700) can both give rise to these experimental peaks.[71] Their coexistence likely reflects long-range disorder in cation distribution and layer stacking, typical for M^{2+} - M^{3+} LDHs.[70,71] Additionally, the peaks at 19.6°, 38.3°, 50.7°, 62.1°, 69.0° and 81.3° suggest the presence of brucite ($Mg(OH)_2$, PDF card 01−1169), though multiple of these reflections overlap with those of the LDH phases. After calcination, a clear signature of an MgO periclase structure is present (PDF card 45−0946), commonly observed when an LDH phase collapses into an $Mg(M^{3+})O_x$ phase.[70−73] No crystalline iron- or aluminum-only phases are discerned, further suggesting these elements are mostly dispersed within the MgO lattice. However, the presence of possible amorphous phases cannot be excluded.

The evolution of LDH phases is further confirmed by in situ monitoring of the crystal phase transformations during the calcination process (Figure 3b), showing two characteristic transitions.[73] The first transition occurs around 420 K as a decrease in peak intensity at 34.2° and 38.3°, typical for dehydration of the LDH material. This is accompanied by a (partial) restructuring of the trivalent cations from an octahedral to tetrahedral coordination, while still preserving the layered structure. The second transition occurs abruptly at 640 K. The LDH peaks at 34.2° and 38.3° disappear and the main MgO peak occurs at 2θ = 42.9°. This is caused by the decomposition of interlayer anions and the concomitant collapse of the layered LDH structure. Above 640 K, the crystal size of this phase increases as the peak width gradually decreases. No intermediate or secondary crystal phases are formed when transitioning from the LDH precursor to the final catalyst material, indicating that the MgO lattice likely contains Fe^{3+} and Al^{3+}, representing a periclase-like $Mg(Fe,Al)O_x$ phase.

3.2. Activity Tests

3.2.1. RWGS Activity. CO_2 can assist in CO_2−PDH through a two-step pathway, in which dehydrogenation (eq 1) is followed by RWGS (eq 2).[2] The RWGS reaction then provides a pathway for in situ H_2 consumption, shifting the dehydrogenation equilibrium toward C_3H_6. It also provides a model reaction for CO_2 activation under redox conditions resembling those of CO_2−PDH. Here, the intrinsic activity of $Mg(Fe,Al)O_x$ for the RWGS reaction is assessed in view of examining its possible effect during CO_2−PDH.

The CO_2 conversion during RWGS and the carbon accumulation after 15 min TOS are shown in Figure 4 for 5 different temperatures, confirming that the $Mg(Fe,Al)O_x$ catalyst does exhibit RWGS activity. Both CO_2 and H_2 (Figure S3) conversions rapidly evolve toward a steady-state in RWGS. The high initial conversions are ascribed to transient effects rather than to thermodynamics. These transient effects can entail the adsorption of CO_2 on $Mg(Fe,Al)O_x$ surface up to a certain coverage, the reduction and subsequent oxidation of Fe in the catalyst by H_2 and CO_2 (establishing a certain Fe^{3+} vs Fe^{2+} ratio), and possible pressure effects upon switching of the gas feed valves. The CO_2 conversion profile is relatively stable within the 873 K − 973 K temperature range and at the employed $W_{cat}{\cdot}F^0{}_{tot}{}^{-1}$ = of 1.8 $kg_{cat}{\cdot}s{\cdot}mol^{-1}$. The CO_2 conversions after 15 min range from 37% to 13%, each time remaining below the corresponding equilibrium conversion. The H_2 conversion profile (SI, Figure S3) follows that of CO_2 both in shape and magnitude, with quasi-constant CO_2:H_2 conversion ratios within a reaction run. The carbon accumulation after 15 min TOS is negligible, with values on

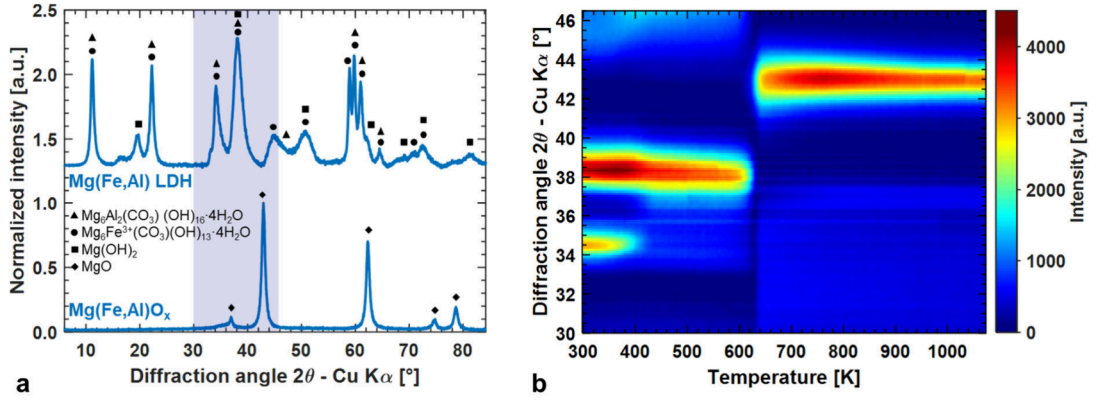

Figure 3. XRD for $Mg(Fe,Al)O_x$ synthesis verification, measured at Cu K_a energy. **a)** Full XRD patterns of the LDH precursor (top) and the $Mg(Fe,Al)O_x$ catalyst (bottom) obtained after 5 h calcination in air at 1073 K. Patterns recorded at RT in air, baseline subtracted, and individually normalized for the most intense peak. The shaded region indicates the 2θ range shown in panel b). **b)** In situ XRD patterns during calcination of the LDH precursor. Patterns are baseline-subtracted. Flow: 200 N ml·min^{-1} air. Temperature program: 5 K·min^{-1} linear ramp from 300 to 1073 K, without dwell.

https://doi.org/10.1021/acscatal.5c09151
ACS Catal. 2026, 16, 3999−4016

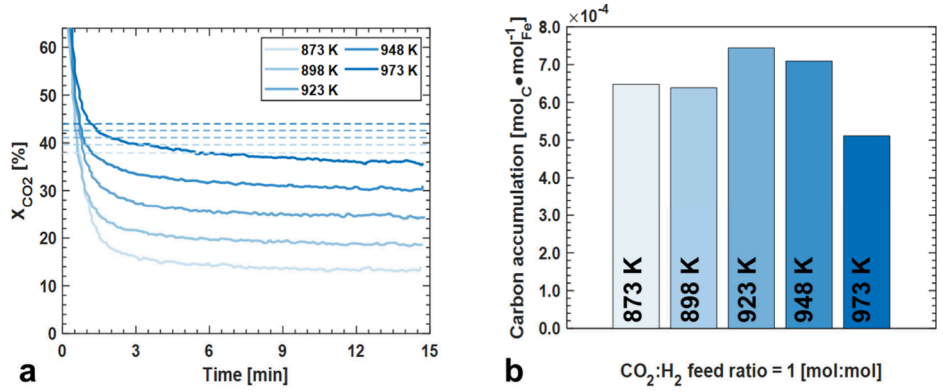

Figure 4. RWGS reaction over Mg(Fe,Al)O_x at equimolar CO_2:H_8 feed ratios. Tests performed isothermally at 121.3 kPa and at $W_{cat} \cdot F^0_{tot}{}^{-1}$ = 1.8 $kg_{cat} \cdot s \cdot mol^{-1}$. Temperature increases from light to dark colors. **a**) CO_2 conversion for different temperatures. Dashed lines show equilibrium conversions. **b**) Carbon accumulation after 15 min TOS.

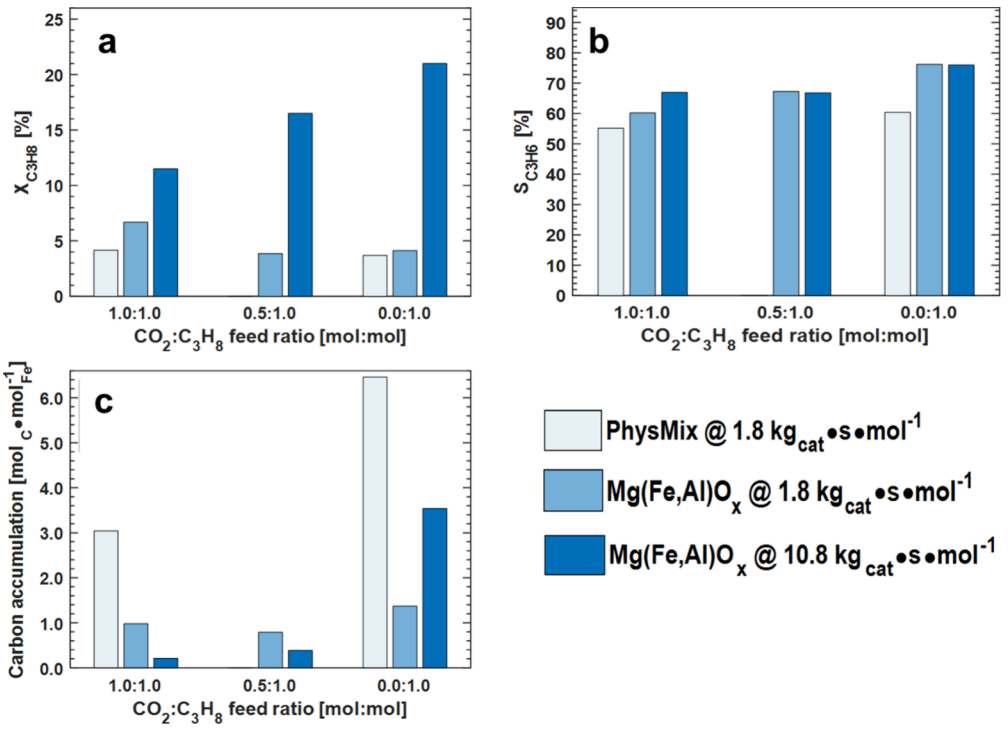

Figure 5. Catalytic activity parameters during (CO_2-)PDH using different CO_2:C_3H_8 feed ratios. Tests performed at 873 K, 121.3 kPa, and at $W_{cat} \cdot F^0_{tot}{}^{-1}$ = 1.8 or 10.8 $kg_{cat} \cdot s \cdot mol^{-1}$. "PhysMix" denotes a physical mixture of bulk Fe_2O_3 and MgO with equal Fe:Mg molar ratio as the Mg(Fe,Al)O_x catalyst. **a**) C_3H_8 conversion. **b**) C_3H_6 selectivity. **c**) Carbon accumulation after 20 min TOS. Light to dark colors indicate PhysMix at 1.8 $kg_{cat} \cdot s \cdot mol^{-1}$, Mg(Fe,Al)$O_x$ at at 1.8 $kg_{cat} \cdot s \cdot mol^{-}$,[1]and Mg(Fe,Al)$O_x$ at 10.8 $kg_{cat} \cdot s \cdot mol^{-1}$, respectively.

the order of $6 \cdot 10^{-4}$ mol C per mol Fe. No CH_4 formation was observed.

Figure 4a shows that CO_2 can be effectively activated and reduced on the Mg(Fe,Al)O_x sample under relevant high-temperature redox conditions. This directly supports the idea that, in CO_2–PDH, (part of the) CO_2 consumption can proceed via H_2-assisted CO_2 reduction (RWGS), next to other parallel reactions ($Fe^{3+} \leftrightarrow Fe^{2+}$ and carbon oxidation). The RWGS activity of the current Mg(Fe,Al)O_x sample is comparable to that of other FeO_x- and Fe-metal-based catalysts in the context of CO_2-assisted dehydrogenation.[21,24,45,74,75] However, this Mg(Fe,Al)O_x is still outperformed by Pt–Sn and Pt–In catalysts examined in prior work, which readily reached equilibrium CO_2 conversions at equimolar CO_2:H_2 feeds.[17] This was achieved by impregnating 3 wt % of Pt and promoter (Sn or In) onto a spinel $MgAl_2O_4$ with similar porosity characteristics as the present Mg(Fe,Al)O_x.

3.2.2. CO_2–PDH Activity. The performance of the LDH-derived Mg(Fe,Al)O_x during (CO_2)-PDH at 873 K is shown in Figure 5 for different CO_2:C_3H_8 feed ratios, and compared to a physical mixture of bulk Fe_2O_3 and MgO with a molar Fe:Mg ratio equal to that of the catalyst. The propane conversion is highest without CO_2 and decreases with CO_2 increase, reflecting the competition of both molecules for the available adsorption sites. In presence of CO_2, H_2 will get removed through RWGS, as confirmed by the RWGS activity (Figure 4a), hence shifting equilibrium. However, not all CO_2 is available for this shift, since it will also be consumed by C oxidation and Fe^{2+} reoxidation.

https://doi.org/10.1021/acscatal.5c09151
ACS Catal. 2026, 16, 3999–4016

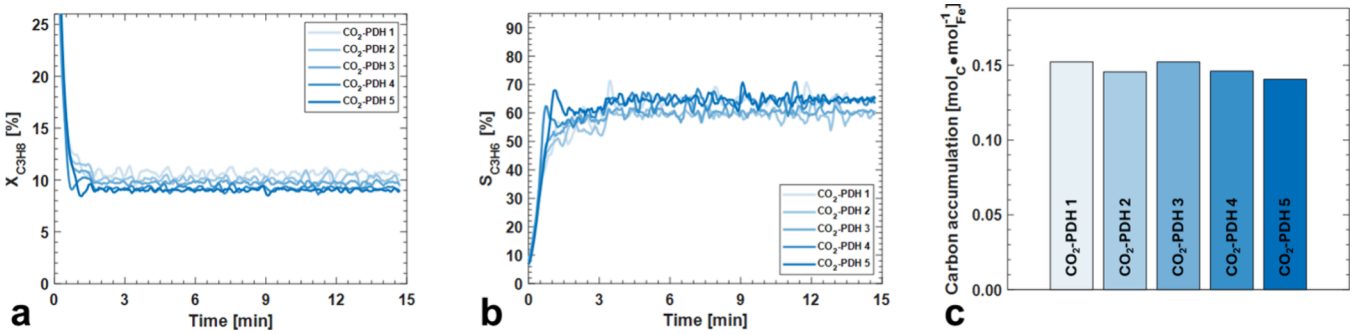

Figure 6. Repeated CO_2−PDH on Mg(Fe,Al)O_x with equimolar CO_2:C_3H_8 feed ratio, with 20 min isothermal O_2 regeneration in between reactions. Tests performed at 873 K, 121.3 kPa, and $W_{cat}{\cdot}F^0{}_{tot}{}^{-1}$ = 10.8 $kg_{cat}{\cdot}s{\cdot}mol^{-1}$. **a)** C_3H_8 conversion. **b)** C_3H_6 selectivity. **c)** Carbon accumulation after 15 min TOS. Light to dark colors indicate an increasing number of CO_2−PDH − O_2 regeneration cycles.

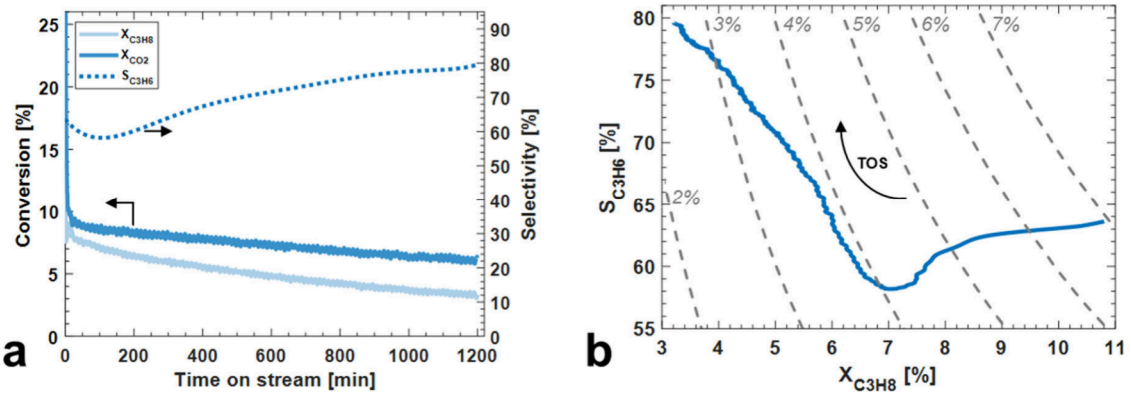

Figure 7. CO_2−PDH 20 h TOS stability test of Mg(Fe,Al)O_x. Tests performed at 873 K, 121.3 kPa, and $W_{cat}{\cdot}F^0{}_{tot}{}^{-1}$ = 10.8 $kg_{cat}{\cdot}s{\cdot}mol^{-1}$. **a)** C_3H_8 conversion (left axis), CO_2 conversion (left axis) and C_3H_6 selectivity (dotted, right axis). **b)** C_3H_6 selectivity and CO_2:C_3H_8 conversion ratio plotted against C_3H_8 conversion. Iso-yield contours for propylene are shown with dashed gray lines.

Mg(Fe,Al)O_x shows higher C_3H_6 selectivities and lower carbon accumulation than the physical mixture. Given the importance of $Fe^{\delta+}$ dispersion for C−H bond selectivity, these results further confirm that Fe in the Mg(Fe,Al)O_x sample is well-dispersed. Moreover, nonoxidative PDH and CO_2−PDH over the physical mixture yield similar C_3H_8 conversion and C_3H_6 selectivity, while the carbon accumulation halves during CO_2−PDH. This implies that the presence of CO_2 does not alter the nature of the active Fe sites on bulk FeO_x. Rather, CO_2 assists in the oxidation of carbon. causing a significant reduction of carbon over the Mg(Fe,Al)O_x catalyst (Figure5c). This effect is more pronounced at higher $W_{cat}{\cdot}F^0{}_{tot}{}^{-1}$. However, the C_3H_8 conversion and C_3H_6 selectivity do not follow the same trend. In absence of CO_2, the C_3H_6 selectivity is even higher. This can be caused by competitive adsorption between CO_2 and C_3H_8 on selective Fe sites, or by changed Fe properties due to a CO_2−C_3H_8 redox interplay. Overall, the Fe-TY of the Mg(Fe,Al)O_x catalyst shown in Figure 5 lies between 2.0 and 5.6 $mmol_{C3H6}{\cdot}mol_{Fe}{}^{-1}{\cdot}s^{-1}$, placing it among the best-performing Fe-based CO_2−PDH catalysts (Table S1). This is comparable to the works of Theofanidis et al.[45] and Michorczyk et al.,[32] although still below what has been achieved for nonoxidative PDH.[28]

The catalytic stability across reaction-regeneration cycles was assessed by repeating 5 CO_2−PDH reactions of 15 min at a $W_{cat}{\cdot}F^0{}_{tot}{}^{-1}$ of 10.8 $kg_{cat}{\cdot}s{\cdot}mol^{-1}$ and equimolar CO_2:C_3H_8 feed ratios, using 20 min O_2/Ar regenerations in between. The resulting conversion profiles for C_3H_8 and CO_2 are stable across the 5 regeneration cycles, both maintaining values around ∼ 10% (Figure 6). The C_3H_6 selectivity also shows consistent profiles across regeneration cycles and rises to 65%. In contrast to the Pt−Sn and Pt−In catalysts examined in prior work,[17] repeated exposure to reaction-regeneration conditions does not influence the initial activity of the Mg(Fe,Al)O_x catalyst.

The effect of prolonged exposure to CO_2−PDH was assessed in a 20 h TOS stability test. Catalyst deactivation is observed as the C_3H_8 conversion dropped from 10.7% to 3.3% (Figure 7a), while the CO_2 conversion decreased from 11.3% to 6.2%. The CO_2 conversion being higher than the one of C_3H_8 could result from a combined effect of RWGS, dry reforming of C_3H_8 (requiring 3 mol of CO_2 per mole of C_3H_8), hydrocarbon oxidation through $Fe^{3+} \rightleftharpoons Fe^{2+}$ cycling (e.g., for C_3H_8: requiring 1 or more moles of CO_2 per mole of C_3H_8), and carbon gasification.

The carbon accumulation after 20 h TOS amounted to 6.95 mol C per mol Fe. While the C_3H_8 and CO_2 conversions consistently decrease, the C_3H_6 selectivity reaches a minimum of 58.2% before increasing to a final value of 78.9% (Figure 7b). This minimum is also present when plotting C_3H_6 selectivity vs C_3H_8 conversion, with different slopes on each side of this minimum. These different regimes may pertain to distinct carbon formation regimes and/or different speciations of Fe within the mixed oxide matrix. Furthermore, the C_3H_6 selectivity value after 20 h TOS lies close to that of nonoxidative PDH with minute-scale TOS (Figure 5a). These results suggest that the presence of CO_2 slows down a material transition that occurs more rapidly in nonoxidative

https://doi.org/10.1021/acscatal.5c09151
ACS Catal. 2026, 16, 3999−4016

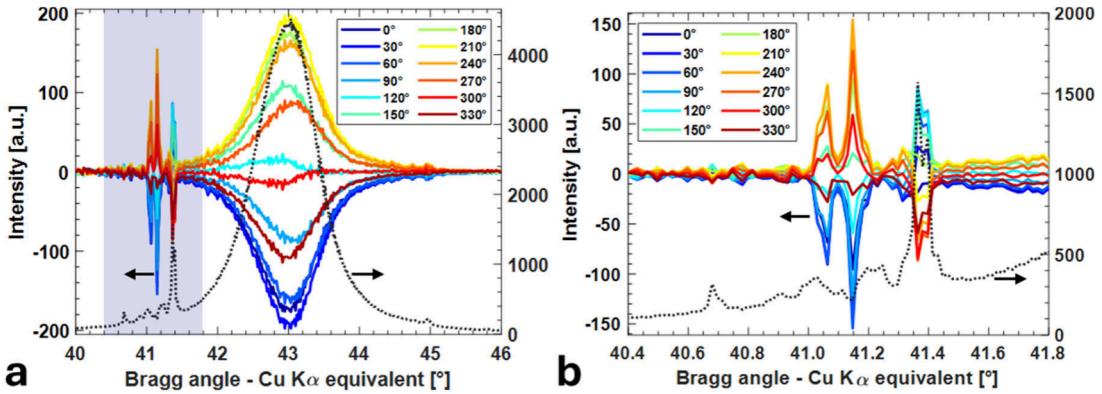

Figure 8. PSD results at k = 3 for CO_2−H_2 ME-XRD on Mg(Fe,Al)O_x. Square wave ME program at 973 K according to Figure 1d. **a)** Demodulated diffraction vs Bragg angle, with overlay of the pattern of principal component 1 (dotted line). The shaded region indicates the 2θ range shown in panel b). **b)** Detail of the demodulated diffraction.

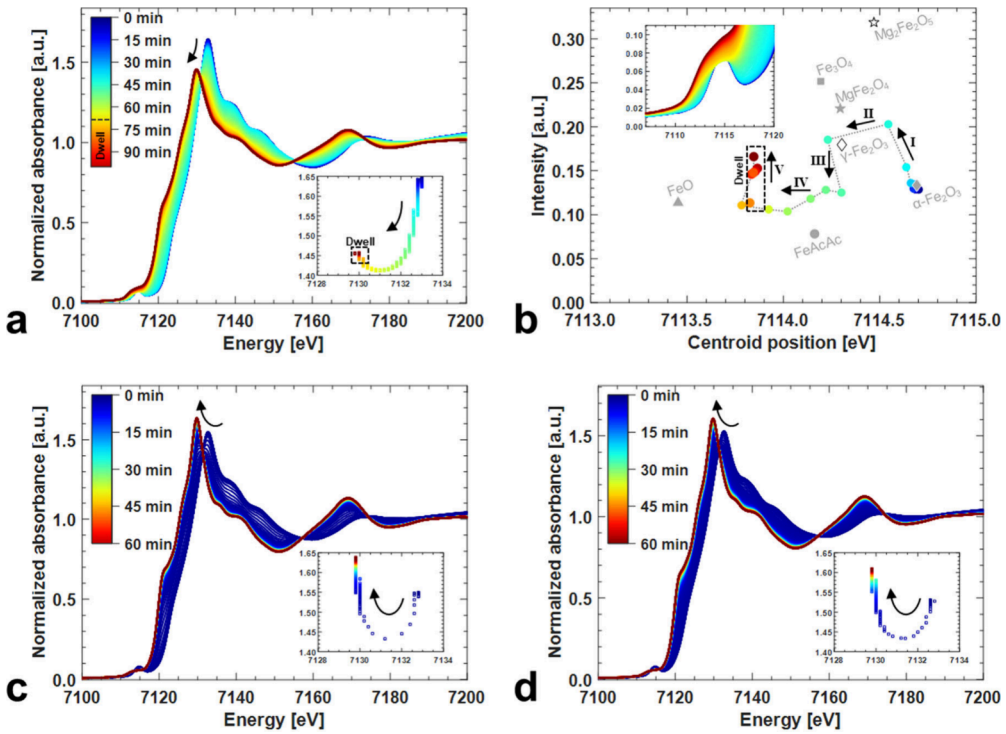

Figure 9. Time-resolved in situ XANES profiles at the Fe K-edge for Mg(Fe,Al)O_x. Each experiment was preceded by an O_2 treatment at 973 K. Arrows indicate the course of the experiment. **a)** H_2-TPR from 300 to 973 K (10 K·min^{-1}, 30 min dwell) under 1.4 N ml·min^{-1} H_2 and 5.6 N ml·min^{-1} He. Inset: evolution of white line intensity and position. **b)** Pre-edge variogram of the H_2-TPR experiment (integrated pre-edge intensity vs centroid position), along with measured references. Inset: XANES detail around the pre-edge region. **c)** RWGS at 973 K under 1.4 N ml·min^{-1} H_2, 1.4 N ml·min^{-1} CO_2 and 4.2 N ml·min^{-1} He. Inset: evolution of white line intensity and position. **d)** CO_2−PDH at 973 K under 1.4 N ml·min^{-1} C_3H_8, 1.4 N ml·min^{-1} CO_2 and 4.2 N ml·min^{-1} He. Inset: evolution of white line intensity and position.

PDH. To further detail such material transitions, in situ characterization is applied.

3.3. In Situ X-ray Characterization

3.3.1. Crystalline Material Restructuring through XRD. Crystalline material transitions were assessed through in situ XRD at 9686.9 eV (cfr. Figure 1b). The diffraction patterns obtained after O_2-TPO, CO_2−PDH, CO_2 and O_2 regeneration treatments are all dominated by reflections of the periclase-like Mg(Fe,Al)O_x (SI, Figure S6a). The different treatments, however, give rise to small variations in position and relative intensity of these reflections, suggesting the treatments induce small changes to this crystal lattice. Additionally, a set of narrow peaks is present in all patterns. Since these peaks do not correspond to periclase structures, but do appear in the diffraction pattern of a measured MgO reference material, they are attributed to background contributions (SI, Figure S6b). As with lab-based Cu K_α radiation (Figure 3), no separate iron-only phases are discerned at 9686.9 eV.

To resolve possible substructures causing the small changes in the periclase-like reflections, ME-XRD was applied using a square wave CO_2−H_2 concentration modulation with 6 min periods at 973 K, coupled with PSD analysis.[38,49] This work presents a first-of-a-kind application of ME-XRD at the ESRF ID20 beamline. Prior to PSD, the obtained time-resolved diffraction patterns were normalized against the invariant

https://doi.org/10.1021/acscatal.5c09151
ACS Catal. 2026, 16, 3999−4016

background peaks and subsequently averaged within the QSS regime into one period (SI, Figure S7). This modulation protocol balanced the time resolution of the XRD setup with the sampling rate requirements for a reliable PSD analysis, while trying to avoid complete bulk responses of the material (see section 2.3.1.2).[38] It should be noted that PSD on diffraction intensities only separates a responsive substructure from passive contributions at $k = 2$.[50,76] Square wave modulations lack the $k = 2$ harmonic (SI, Figure S7c), but the resembling envelope shapes at $k = 1$ (SI, Figure S8) and $k = 3$ (Figure 8) suggest that a similar response would have been observed at the $k = 2$ harmonic, had it been accessible.[50,77]

Figure 8a shows the demodulated diffraction at $k = 3$, revealing changes of the MgO(200) reflection in terms of position and intensity. The subtle angular shifts of the PSD maximum around 43° could point to $Fe^{3+} \rightleftharpoons Fe^{2+}$ transitions within the periclase-like lattice of $Mg(Fe,Al)O_x$ and/or $Fe^{\delta+}$ moving in and out of this lattice. Alternatively, partial transitions between $Mg(Fe,Al)O_x$ and spinel phases like $MgAl_2O_4$ or $MgFe_2O_4$ are possible (SI, Figure S7a). In addition, small contributions between 41.0° and 41.5° are visible, detailed in Figure 8b. These features do not align with the narrow background peaks and could be ascribed to FeO(200) planes (PDF cards 69−0687). No variations occur at the position of the main diffraction peak of metallic Fe^0 (~44.7°), meaning there is no metallic Fe involved in the discerned transitions. These results suggest that redox environments corresponding to RWGS conditions extract and reincorporate a fraction of $Fe^{\delta+}$ species from an $Mg(Fe,Al)O_x$ periclase-like matrix. The local environment of these $Fe^{\delta+}$ species is further detailed through QXAS.

3.3.2. Local Material Restructuring through QXAS. To identify the local material restructuring around Fe, a stepwise approach is taken, going from reducing conditions (H_2-TPR) over RWGS (feed of H_2 and CO_2) to CO_2−PDH (reactive feed of C_3H_8 and CO_2). Figure 9 shows the spectral variations at the Fe K-edge of $Mg(Fe,Al)O_x$ for these consecutive treatments. The numerical values of the white line (WL) are listed in SI Table S3. Spectra of references and selected overlays are shown in the SI, Figure S9. In what follows, the term "*saddle point*" refers to the state of minimal WL intensity within a spectral evolution, a feature observed in all in situ treatments.

3.3.2.1. Properties during H_2-TPR. Figure 9a shows the XANES evolution during H_2-TPR. The WL shifts toward a lower intensity and lower energy position, while passing through a "*saddle point*": from 1.65 at 7133.0 eV through 1.41 at 7130.8 eV to 1.46 at 7129.8 eV. The "*saddle point*" spectrum during H_2-TPR shows close but incomplete resemblance to the Fe_3O_4 reference (SI, Figure S9c), suggesting the reduction proceeds through a comparable intermediate. The final H_2-TPR spectrum does not match any of the bulk references, such as Fe_3O_4, FeO, or Fe foil (SI, Figure S9 and Table S3). Linear combination fitting using $MgFe_2O_4$, $Mg_2Fe_2O_5$, α-Fe_2O_3, γ-Fe_2O_3, Fe_3O_4, FeO and Fe foil could not adequately replicate the combination of WL position, WL intensity and pre-edge shape. Starting from ab initio XANES simulations of bulk references (SI, section 8.2, Figure S10) to set simulation parameters, several hypothesized structures were evaluated for XANES simulation of the reduced $Mg(Fe,Al)O_x$ sample (Table S4). No resemblance was found between simulations and experiment, excluding the bulk references as possible structure for the reduced $Mg(Fe,Al)O_x$ sample. Hence, the average local Fe environment in $Mg(Fe,Al)O_x$, derived from LDH, differs from pure periclase or spinel. Rather, Fe may still be (partially) incorporated in the mixed oxide matrix after reduction, and hence only partially reduced.

Besides the WL, also the pre-edge changes notably during H_2-TPR (inset of Figure 9b). The Fe K pre-edge feature arises from 1s→3d transitions, dominated by dipole components.[78,79] Theoretically, the latter are forbidden in centrosymmetric environments, e.g. when Fe occupies the octahedral inversion center in an MgO lattice. In practice, however, this centrosymmetry can be partially disrupted by asymmetric vibrations, e.g. local distortions, leading to an increased pre-edge intensity.[80] Deconvoluting the Fe K pre-edge feature allows to resolve coordination (~intensity) from oxidation state (~energy position or centroid position).[60,78,81,82] Hereto, the pre-edge features in H_2-TPR were fitted via pseudo-Voigt peaks. Contributions centered above 7115.0 eV stem from nonlocal interactions and were excluded from the analysis.[60,78,81] Figure 9b shows the results throughout the H_2-TPR treatment as a variogram, along with several bulk references. A first change (I) occurs at ~ 573 K, where the pre-edge intensity rapidly rises and the centroid position is lowered by 0.2 eV. The elevated intensity indicates a more tetrahedral-like nature of the Fe environment, while the centroid position still implies a dominant Fe^{3+} character.[60,78,81] A second shift (II) occurs at ~ 693 K, with a rapid decrease in centroid position toward an $Fe^{3+/2+}$ state, while maintaining the partial tetrahedral character. When further increasing the temperature (III), the intensity lowers, indicating a return to octahedral character at 823 K. When reaching 973 K (IV), an average Fe phase is obtained with octahedral character and an oxidation state close to Fe^{2+}. Such a material evolution aligns with findings from De Coster et al. for $MgFe_xAl_{1-x}O_4$ spinel phases.[83] Finally, the 30 min dwell at 973 K (V) does not change the oxidation state but again increases the tetrahedral character. These findings also align with the reduction evolution shown by an MCR-ALS analysis using 5 principal components (SI, Figure S12−S13), and with the H_2 consumption profile during a similar conventional H_2-TPR treatment (SI, Figure S15).

3.3.2.2. Redox Properties during RWGS and CO_2−PDH. A CO_2-TPO treatment reverses the trends seen during H_2-TPR, again obtaining an Fe^{3+} state (SI, Figure S9a-b). The final XANES spectrum closely resembles that of a more severe O_2-TPO treatment. It is therefore expected that the simultaneous presence of H_2 and CO_2 will induce Fe redox dynamics. This was studied through the RWGS reaction, which provides model redox conditions for CO_2−PDH. Besides probing the material's redox properties, RWGS itself can partake in CO_2−PDH via eq 1 and eq 2.

Figure 9c shows the XANES evolution during RWGS with equimolar CO_2:H_2 feed ratio at 973 K. Under these conditions, a rapid WL shift occurs, implying a swift reduction from Fe^{3+} toward Fe^{2+}. This is accompanied by a weakening of the pre-edge feature. The WL passes through a "*saddle point*", closely resembling the one observed during H_2-TPR (Table S3).

The XANES evolution during a true CO_2−PDH environment, involving alkane transformations, is shown in Figure 9d. A similar evolution is observed as in the model redox conditions of RWGS, with a rapid WL shift to lower energies while passing through a saddle point. Together with ME-XRD under H_2/CO_2 modulation (Figure 8), indicating a reversible, CO_2-responsive Fe population that can be extracted from and

https://doi.org/10.1021/acscatal.5c09151
ACS Catal. 2026, 16, 3999−4016

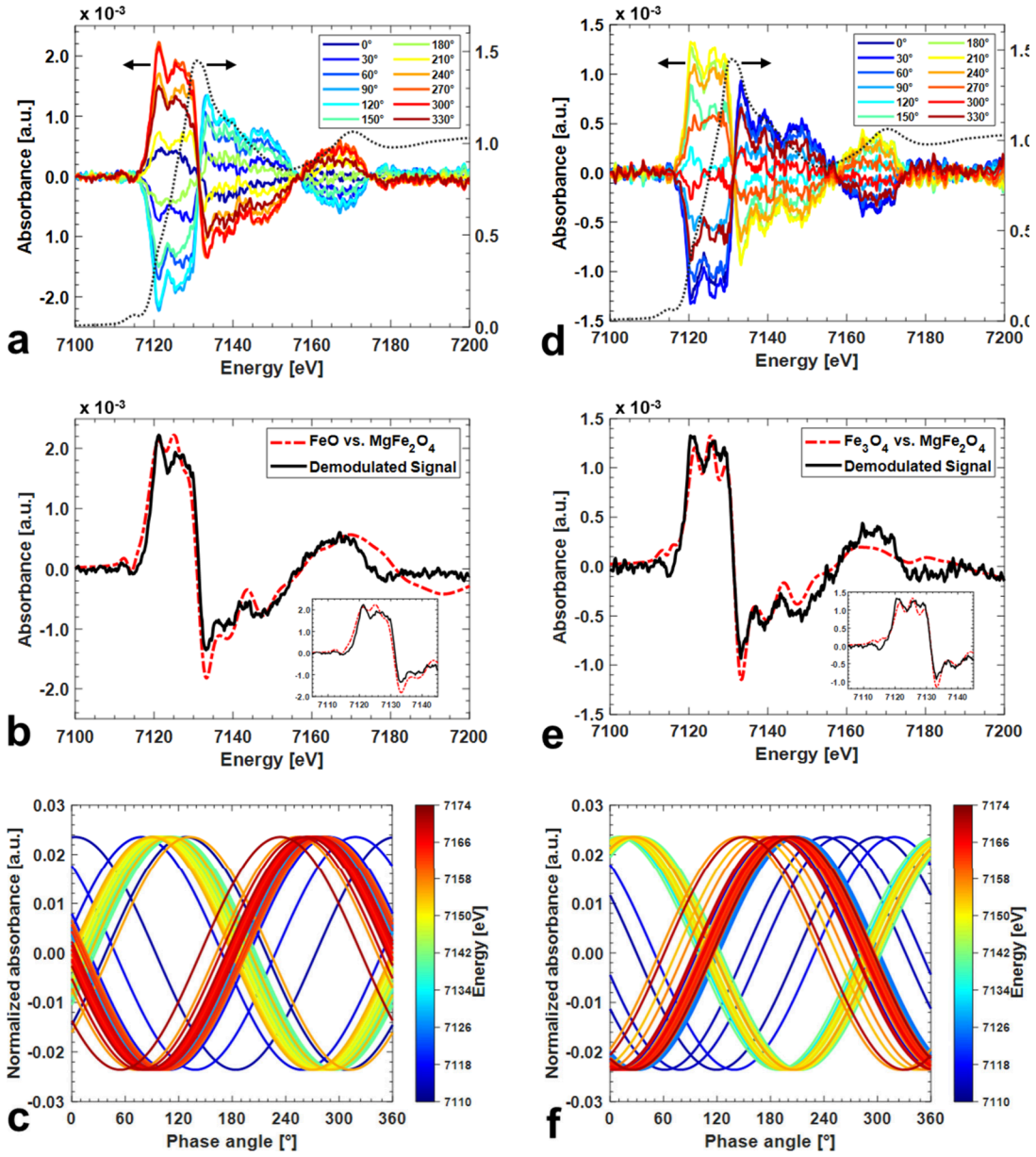

Figure 10. PSD results of CO_2−C_3H_8 ME-XAS at the Fe K-edge of $Mg(Fe,Al)O_x$. Rectangular wave ME program at 873 K according to Figure 1e. **a**) Demodulated absorbance vs energy at k = 1, with XANES overlay of the principal component dominant during the quasi steady-state regime (dotted line). **b**) In-phase spectrum at k = 1 (φ_1^{PSD} = 270°) and difference spectrum of FeO vs $MgFe_2O_4$ references. **c**) Demodulated absorbance vs phase angle for k = 1 (φ_1^{PSD}). **d**) Demodulated absorbance vs energy at k = 2, with XANES overlay of the principal component dominant during the quasi-steady state regime (dotted line). **e**) In-phase spectrum at k = 2 (φ_2^{PSD} = 210°) and difference spectrum of Fe_3O_4 vs $MgFe_2O_4$ references. **f**) Demodulated absorbance vs phase angle for k = 2 (φ_2^{PSD}).

reincorporated into the $Mg(Fe,Al)O_x$ matrix, these XANES results show that RWGS conditions (Figure 9c) probe the same Fe^{3+}/Fe^{2+} redox couple that operates during CO_2−PDH (Figure 9d), thereby validating the catalyst's ability to undergo CO_2-coupled redox cycling.

Comparing all WL shifts in Figure 9 reveals a similar saddle point for all treatments, and the spectra at that point each time resemble the XANES profile of the Fe_3O_4 reference (Figure S9c). The final spectra all have a WL and pre-edge that point to the formation of Fe^{2+} species (SI, Figure S9a-b). Beyond the saddle point, the WL intensity increases, and the WL shape is notably sharper than that of the bulk FeO reference material. This implies different local or nonlocal Fe^{2+} environments are obtained in $Mg(Fe,Al)O_x$. The WL increase is more pronounced in the redox environments of RWGS and CO_2−PDH than in H_2-TPR. Hence, the presence of CO_2 can affect both the local and nonlocal Fe^{2+} environment within $Mg(Fe,Al)O_x$.[84]

3.3.2.3. EXAFS Analysis. To complement the preliminary insight into the Fe oxidation states and coordination environments, EXAFS analysis was performed to probe the local structure around Fe species after the different redox and reactive treatments (SI, Table S5 and Figure S11). The R-space profiles show moderate changes across treatments. Resemblances are found in R-space between the as-prepared and post CO_2-TPO states, featuring two similar peaks at ∼ 1.6 and ∼ 2.6 Å (not phase-corrected), albeit with different intensity ratio, as well as similar imaginary parts of the Fourier

https://doi.org/10.1021/acscatal.5c09151
ACS Catal. 2026, 16, 3999−4016

transform. Other resemblances are found between the post H_2-TPR and post ME-XAS states in R-space, showing a lower first-shell peak at ∼ 1.5 Å and second-shell peak at ∼ 2.6 Å. Additionally, a shoulder emerges at ∼ 1.8 Å, which is most pronounced after the H_2-TPR treatment.

For all sample treatments, comparing fits with different crystal phases to the R-space magnitude and imaginary part yielded a best fit with mixed Mg−Fe oxides. Adding partial or full contributions of bulk Fe oxide phases or metallic Fe phases resulted in high R-factors (>8%) and physically meaningless parameters.

Fitting the as-prepared state with effective scattering paths for an $Mg_{0.6}Fe_{0.4}O$ structure yields an Fe−O coordination number of 5.0 ± 0.3, which could point to a locally distorted octahedral coordination, in agreement with the pre-edge analysis. The fitted Fe−O bond distance is 1.974 ± 0.005 Å. This is slightly shorter than that of a Mg^{2+}-O bond in a periclase structure, which could be attributed to the smaller ionic radius of Fe^{3+} (60 pm vs 72 pm effective radius).[85] Fitting of the second shell reveals a mixed contribution of Fe and Mg, with a sample-averaged Fe−Fe coordination number of ∼ 8 and Fe−Mg coordination number of ∼ 4. It is to be noted that the Debye−Waller factor for the Fe−Fe path is high, which again points to a distorted local environment. This supports the provisional observations of Fe being incorporated as Fe^{3+} in a periclase $Mg(Fe,Al)O_x$ lattice environment. However, given the Fe−Fe coordination number, the actual distribution of oxidized Fe species likely occurs as subnanometre clusters with (XRD-) amorphous character, rather than as atomically dispersed species.

Fitting the post H_2-TPR spectrum with only $Mg_{0.6}Fe_{0.4}O$ resulted in insufficient match (R = 9.04%), indicating an additional path was required. Hence, an extra tetrahedral Fe−O path from $MgFe_2O_4$ was added, yielding a better fit (R = 2.66%). This increased tetrahedral character aligns with the pre-edge analysis (see Figure 9b). Given that Fe^{2+} has a larger radius than Fe^{3+} (70 pm vs 60 pm effective radius, respectively),[85] the increased bond distance of the octahedral Fe site after reduction, 2.035 vs 1.974 Å, could point to Fe^{3+} being reduced to Fe^{2+} within the $Mg(Fe,Al)O_x$ periclase environment.[85] Compared to the as-prepared material, a relatively higher Mg coordination number is obtained for the second shell: 5.7 vs 3.8. This analysis thus indicates a partial restructuring of the material into two different Fe-containing oxide environments.

The post CO_2-TPO spectrum can be well fitted with $Mg_{0.6}Fe_{0.4}O$, leading to similar conclusions as those made for the as-prepared state. Likely, any Fe that previously migrated is now being reincorporated as Fe^{3+} into the periclase-like lattice of $Mg(Fe,Al)O_x$. However, the Debye−Waller factor for the second-shell Fe−Fe path has decreased, which indicates that the lattice upon reincorporation now yields a more structured or crystalline phase.

Finally, EXAFS fitting of the post CO_2−PDH ME-XAS spectrum (see section 3.3.3) leads to similar conclusions as the post-H_2-TPR spectrum, with minor tetrahedral Fe−O contributions existing alongside an octahedral Fe−O environment. Hence, CO_2−PDH ME-XAS entails similar structural changes to those observed in H_2-TPR on the sample-averaged level. This comprises the emergence of local $MgFe_2O_4$-like signatures, with $Fe^{\delta+}$ in tetrahedral configuration, parallel to the dominant $Mg_{0.6}Fe_{0.4}O$, where $Fe^{\delta+}$ is octahedrally surrounded.

Overall, the EXAFS results align with XANES and XRD, supporting a redox-responsive Fe environment characterized by dominant octahedral $Fe^{3+} \rightleftharpoons Fe^{2+}$ transformations, and minor formation of tetrahedral $Fe^{\delta+}$. Again, no contributions of metallic Fe are discerned, suggesting that all Fe is successfully immobilized in the $Mg(Fe,Al)O_x$ catalyst.

3.3.3. Responsive Fe Species through ME-XAS. Modulation-excitation QXAS with CO_2−C_3H_8 modulations at 873 K was performed to elucidate the nature of the Fe species participating in the CO_2−PDH reaction (Figure 1c,e). The time-resolved ME-XAS spectra at 873 K (SI, Figure S17a) evolve similarly as during the steady-state CO_2−PDH at 973 K, but now the WL stabilizes closer to the "*saddle point*". Namely, a WL shift occurs from 7132.8 to 7130.8 eV with a final intensity of 1.45 (Table S3). For the post ME-XAS state, EXAFS analysis revealed a dominant octahedral and minor tetrahedral Fe environment on a sample-averaged level (section 3.3.2.3). MCR-ALS is performed with 2 principal components to determine the QSS regime. Their concentration profiles exhibit periodic oscillations that evolve asymptotically to 100% and 0%. (SI, Figure S17e). Analyzing the frequency content of the latter through a single-sided fast Fourier transform reveals the presence of 0.00417 s^{-1} and 0.00833 s^{-1}, corresponding to the first and second harmonic frequency of the imposed modulation period of 240 s (SI, Figure S17d).[86]

The phase-resolved spectra from the QSS are plotted vs energy and vs phase angle (φ_k^{PSD}) in Figure 10, revealing more variation than the time-resolved spectra, since now only reactive Fe species are being probed. PSD analysis at k = 1 shows a double feature near the Fe edge: a sharp peak at 7121.2 eV and a broader one around 7125.4 eV. Both have an in-phase angle of 270°, meaning the lag vs the stimulus equals 360° - 270° = 90°. An anticorrelated feature appears around the WL (7133.0 eV) with an in-phase angle of 90°. Finally, a faint feature is observed at the pre-edge (7113.8 eV) with an in-phase angle of 120°. In other work, a similar spectral envelope has been attributed to $Fe^{3+} \rightleftharpoons Fe^{2+}$ transitions based on XANES fingerprinting.[44] Along the same line, a difference spectrum between the $MgFe_2O_4$ and FeO references, representative of Fe^{3+} and Fe^{2+} environments, yields the best match with the current in-phase spectrum (Figure 10b), in terms of the coefficient of determination, root-mean-square error and alignment with the double feature at 7121.2 and 7125.4 eV.

Furthermore, three isosbestic points are present in Figure 10a: at 7131.4 eV, 7156.6 and 7175.0 eV. This implies that the demodulated spectral envelope is identical across all phase angles. Hence, a single type of transition between two states is captured in PSD at k = 1, best described with $MgFe_2O_4$ and FeO as boundaries, where the latter is not to be considered a bulk phase, but rather representative of Fe−O paths (Figure 10b). Figure 10c shows the same demodulated absorbance as Figure 10a, but instead plotted as a function of phase angle, with all sine wave amplitudes normalized (Euclidian norm). If all spectral envelopes were indeed truly identical across all phase angles, these sine waves would perfectly overlap. Instead, Figure 10c shows they are lumped in bands with a ∼ 20° width. The sine waves corresponding to energies where the demodulated absorbance is low (i.e., near the noise level in energy domain, cfr. Figure 10a) show the greatest spread. This suggests that the observed variation in phase behavior at those energies may stem from signal noise. Another possibility is the

https://doi.org/10.1021/acscatal.5c09151
ACS Catal. 2026, 16, 3999−4016

contribution of a minority of parallel Fe transitions, as these could induce slight changes to the spectral envelopes.[50]

Analysis at $k = 2$ can reveal possible Fe transitions with comparably faster kinetics that remain unnoticed at $k = 1$.[50,87] The spectral envelopes at $k = 2$ are indeed different, now showing a triple feature near the Fe edge: 7121.2, 7126.6 and 7129.0 eV with an in-phase angle of 210° (Figure 10d). The difference spectrum best describing these three peaks is now obtained from the $MgFe_2O_4$ and Fe_3O_4 references (Figure 10e). According to eq 5, the in-phase angle of 210° should now be considered relative to a periodic function with a frequency of $2 \cdot 2\pi/\tau$ (see also SI, Figure S17c). The different phase lags and spectral envelopes at $k = 1$ vs $k = 2$ confirm that different processes are captured at the different demodulation frequencies.[50,58] Plotting against the phase angle at $k = 2$ (Figure 10f) reveals similar bands of sine waves, again implying a contribution of noise and/or the occurrence of minor transitions parallel to those of $MgFe_2O_4 \rightleftharpoons Fe_3O_4$.

Altogether, ME-XAS identifies the dominant response of $Mg(Fe,Al)O_x$ to CO_2−PDH modulations as Fe^{3+} (best described as $MgFe_2O_4$) being quickly reduced to an Fe_3O_4-like intermediate before further reducing more slowly toward a Fe−O local environment. Under CO_2, the FeO-like species are reoxidized via an Fe_3O_4-like intermediate to Fe^{3+}, with reincorporation into an $MgFe_2O_4$-like phase. Besides this dominant response, the existence of minor parallel pathways is hinted at by the spread in spectral shapes.

Importantly, no periodic transitions toward bulk-like Fe_2O_3 or deeper reduced phases like Fe_3C or Fe^0 are discerned. An example of an Fe^0 response was reported by De Coster et al. for spinel-based Fe−Ni/$MgAl_2O_4$ dry reforming catalysts, showing clearly different spectral envelopes.[44] As derived by Routh et al., an order-of-magnitude estimate can be made of the participating fraction of Fe atoms based on the magnitude of the PSD signals compared to that of the difference spectrum.[52] This shows that only a minority fraction of ∼1% of all Fe atoms present participate in the CO_2−PDH modulations.

4. DISCUSSION

To construct a mechanistic understanding of the active Fe species in CO_2−PDH, the diverse material transformations observed can now be correlated with the activity results.

Comprehensive in situ X-ray characterization reveals Fe transformations between Fe^{3+} and Fe^{2+} species, predominantly octahedral, within a distorted MgO-type matrix. No deeper reduced Fe species, such as metallic Fe^0 or Fe_3C, could be discerned.[29,88] The absence of Fe^0 phases relates to the incorporation and stabilization of $Fe^{\delta+}$ into the $Mg(Fe,Al)O_x$ catalyst. A similar observation has been made for spinel $MgFe_xAl_{1-x}O_4$ samples.[89]

The $Fe^{3+} \rightleftharpoons Fe^{2+}$ redox dynamics are influenced by the presence of CO_2. Namely, the redox environments of RWGS and CO_2−PDH result in higher final WL intensities than during H_2-TPR (Figure 9 and SI, Table S3), pointing to a lower occupancy of the 4p orbital. This can arise from different local and/or nonlocal environments. The low pre-edge intensities obtained in the redox environments further suggest the prevalence of an octahedral local Fe environment (SI, Figure S9b). This is supported by ME-XRD and EXAFS analysis. The presence of CO_2, therefore, enables $Fe^{\delta+}$ to remain incorporated in the periclase-like lattice of $Mg(Fe,Al)O_x$.

ME-XAS under CO_2−PDH conditions identifies part of the Fe^{3+} as responsive species (Figure 10). C_3H_8 reduces these Fe^{3+} species toward Fe^{2+}, while CO_2 reoxidizes them to Fe^{3+}. Both transitions proceed via an intermediate $Fe^{3+/2+}$ phase. The initial signature of these Fe^{3+} species resembles the one of $MgFe_2O_4$, while the one of the Fe^{2+} response resembles that of FeO, and that of the intermediate $Fe^{3+/2+}$ resembles Fe_3O_4. The presence of an $MgFe_2O_4$-like response aligns with Niedermaier et al., who demonstrated that octahedral Fe^{3+} ions dissolved in MgO nanoparticles can segregate toward a minority $MgFe_2O_4$ surface phase at elevated temperatures in air.[82] The driving force for this segregation was attributed to the different oxidation states and ionic radii of Fe^{3+} and Mg^{2+}, thus introducing defect clusters into the material. Such analysis agrees with the current EXAFS fits, which require a minority $MgFe_2O_4$ phase to adequately fit the post-CO_2−PDH ME-XAS spectrum (section 3.3.2.3). In the static XRD data, however, no $MgFe_2O_4$ phase was discerned, supporting the fact that the $MgFe_2O_4$-like response during ME-XAS stems from a minority and/or disordered phase. By the same reasoning, the Fe_3O_4-like and FeO-like ME-XAS responses are likewise attributed to minority and/or disordered phases.

ME-XRD discerns a periodic response of the MgO-type material during H_2−CO_2 modulations (Figure 8). This was attributed to periodic changes of the incorporation and/or oxidation state of $Fe^{\delta+}$ species within this matrix. Similarly, Ferri et al. successfully resolved responses from minority phases in a 2 wt % Pd on $Ce_{0.62}Zr_{0.38}O$ catalyst via ME-XRD.[90] These included responses of Pd phases as well as $Ce^{4+} \rightleftharpoons Ce^{3+}$ changes stemming from only 6 mol % of the total Ce content.

Additional catalyst dynamics can be inferred from the catalytic performance. During nonoxidative PDH, Fe^{3+} species will rapidly reduce to Fe^{2+}, which will persist in the absence of an oxidizing agent. During CO_2−PDH, however, a certain Fe^{3+} vs Fe^{2+} ratio is established within the pool of responsive $Fe^{\delta+}$ species. The higher C_3H_6 selectivity observed in nonoxidative PDH (Figure 5b) therefore implies that Fe^{2+} is the selective site for C−H activation rather than Fe^{3+}. The physical mixture of bulk Fe_2O_3 and MgO is less selective (Figure 5b), in line with literature reporting that aggregated FeO_x phases are nonselective.[26,27,31,33,91] Therefore, although the volume-averaged EXAFS fit indicates some degree of Fe-clustering within the periclase-like matrix (Table S5), the Fe^{2+} sites in $Mg(Fe,Al)O_x$ that selectively promote dehydrogenation then rather appear to be mostly dispersed.

Furthermore, a longer TOS was required during CO_2−PDH to obtain a C_3H_6 selectivity comparable to that of nonoxidative PDH (Figure 7a). It is therefore proposed that the higher Fe^{3+} vs Fe^{2+} ratio enabled by CO_2 initially leads to overoxidation of the hydrocarbons.[92] Another role of CO_2 is to suppress carbon accumulation. The lower carbon content obtained in CO_2−PDH (Figure 5c) points to the $Fe^{3+} \rightleftharpoons Fe^{2+}$ redox couple as a carbon oxidation pathway.

Combining characterization and performance results elucidates two parallel pathways for CO_2−PDH over $Mg(Fe,Al)O_x$, depicted in Figure 11. Because of the observed redox behavior, the concluding mechanistic picture proposed implies only two-step contributions, due to the simultaneous presence of C_3H_8 and CO_2. The one-step mechanism, see eq 3, cannot be excluded, but given the lack of evidence, its contribution is considered limited.

Based on the redox mechanisms observed, i.e. CO_2 consumption and Fe reduction−oxidation, detailed by the

https://doi.org/10.1021/acscatal.5c09151
ACS Catal. 2026, 16, 3999−4016

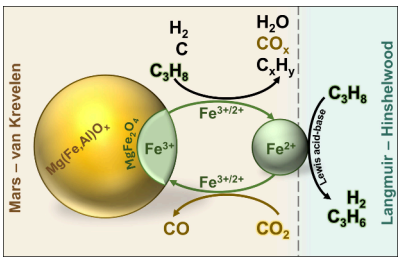

Figure 11. Parallel mechanisms during CO_2−PDH over Mg(Fe,Al)-O_x. In a first pathway (left, Mars − van Krevelen), Fe participates via reversible redox cycling between Fe^{3+} in a surface $MgFe_2O_4$-like phase and dispersed Fe^{2+} species. This cycle can promote carbon removal, but can also lead to overoxidation of propane. In parallel (right, Langmuir − Hinshelwood), the dispersed Fe^{2+} species formed in the Mars − van Krevelen pathway selectively transform propane to propylene and hydrogen via a Langmuir − Hinshelwood-type Lewis acid−base interaction over Fe^{2+} − O^{2-} pairs.

difference spectra from ME-XAS, a first pathway follows a Mars − van Krevelen (MvK) mechanism, in which $Fe^{\delta+}$ reversibly leaves and re-enters a minority $MgFe_2O_4$-like surface phase, forming dispersed Fe^{2+} species via an $Fe^{3+} \rightleftharpoons Fe^{3+/2+} \rightleftharpoons Fe^{2+}$ redox cycle (left-hand panel of Figure 11). Herein, CO_2 primarily contributes through the redox/RWGS functionality—consuming H_2, maintaining the Fe 3+/2+ redox balance, and assisting in coke mitigation. The comparison between nonoxidative PDH and CO_2−PDH implies that this CO_2-enabled redox pathway is only moderately selective for the dehydrogenation of propane (Figure 5b).

In addition, this comparison implies a second, parallel pathway, namely a Langmuir−Hinshelwood−type (LH) dehydrogenation route, in which the dispersed Fe^{2+} species (Fe^{2+}−O^{2-} pairs), formed during the MvK pathway, function as highly selective C−H activation sites that promote propane dehydrogenation. The latter pathway is proposed to occur via Lewis acid−base interactions (right-hand panel of Figure 11), in which a carbon atom from propane can interact with the Lewis acid Fe^{2+} site, while the adjacent hydrogen atom can interact with the Lewis base O^{2-} site. This agrees with work on isolated $Fe^{\delta+}$ sites in zeolite frameworks from Hu et al.[27] and Alghannam et al.[28] Similarly, Lewis acid−base interactions have been described on Zn^{2+} − O^{2-} pairs for nonoxidative propane and *n*-butane dehydrogenation.[93] The LH pathway is hence dominated by Fe^{2+}-site chemistry. However, the dispersed Fe^{2+} as active site for LH can transform to Fe^{3+} upon oxidation by CO_2, ending up in the MvK mechanism.

Based on this mechanistic understanding, catalyst deactivation phenomena can now be assessed by including an analysis of H_2 consumption profiles during repeated H_2-TPR − CO_2-regeneration cycles (see SI, section 9.2). With an increasing number of cycles, the H_2 consumption related to the reduction steps $Fe^{3+} \rightarrow Fe^{3+/2+} \rightarrow Fe^{2+}$ shifts toward lower temperatures. This indicates the formation of more easily reducible FeO_x species, in turn suggesting some extent of FeO_x aggregation that cannot be fully reversed by subsequent oxidation in CO_2 (SI section 9.2.2). However, the impact of this aggregation remains limited after 20 H_2-TPR − CO_2-regeneration cycles, as the corresponding H_2 consumption is still an order of magnitude lower compared to that of a bulk Fe_2O_3−MgO physical mixture. Limited aggregation of $Fe^{\delta+}$ aligns with EXAFS analysis and with STEM-EDX mapping on the corresponding spent sample (SI, Figure S16). Therefore, the Mars − van Krevelen pathway can also yield Fe^{2+} species that are not reincorporated into the spinel upon CO_2 exposure, thus leading to FeO_x aggregation. With prolonged TOS, this aggregation depletes the $MgFe_2O_4$-like surface phase, thereby attenuating the reversible Mars − van Krevelen cycling. Consequently, the pool of dispersed and selective Fe^{2+} species will also diminish. Since aggregated FeO_x species promote C−C bond scission rather than C−H bond scission, such FeO_x species will eventually deactivate through carbon formation. The pool of selective Fe^{2+} sites will decrease in number, but will eventually dominate over the deactivating nonselective Fe^{2+} species. These deactivation pathways are depicted in SI, Figure S19. The aggregate-forming $Fe^{3+} \rightleftharpoons Fe^{3+/2+} \rightleftharpoons Fe^{2+}$ redox transitions (SI, Figure S19) coexisting with the reversible ones of the Mars − van Krevelen cycle (Figure 11) explain the spread in spectral envelopes of the demodulated ME-XAS spectra (Figure 10c,f).

To balance C−H bond selectivity with CO_2 activation and carbon removal, it is therefore not only essential to maintain the dispersion of oxidized Fe species, but also to tune and stabilize the availability of Fe^{3+} vs Fe^{2+}. To this end, further research could focus on optimizing reactor conditions, such as temperature, space time, or the CO_2:C_3H_8 feed ratio. Alternatively, this can be achieved by modifying the catalyst material. For example, the role of Al^{3+} in the dispersion and stability of $Fe^{\delta+}$ species can be further explored. It is known that employing higher concentrations of trivalent metals during the LDH synthesis leads to the formation of long-range spinel structures upon calcination.[94] Tasioula et al. recently showed that a spinel arrangement of Mg, Fe, and Al can stabilize an $Fe^{3+/2+}$ state. The resulting moderated lattice oxygen mobility led to increased C−H bond cleavage selectivity, in contrast to what was observed for purely octahedral Fe^{3+} species.[95]

As a final note, it is worth mentioning that, while Fe^{2+} sites are correlated with higher selectivity, a conclusive assignment of the specific nature of the active site remains to be uncovered. On a sample-averaged level, EXAFS and pre-edge XANES analyses indicate that Fe^{2+} predominantly resides in an octahedral coordination environment. Still, the emergence of minor tetrahedral features under reducing conditions suggests a possible involvement of surface-exposed tetrahedral Fe^{2+} sites. Alternatively, distorted or low-symmetry environments may be involved. The associated Lewis acidity could influence the activation of C_3H_8, as recently suggested for isolated Fe^{3+} in zeolites.[28] Future (site-specific) kinetic studies and DFT modeling could help to resolve the precise local configuration of these selective Fe^{2+} sites.

5. CONCLUSIONS

An LDH-derived Fe-based oxide catalyst was examined for CO_2-assisted PDH. The synthesis route through an LDH precursor enabled the stabilization of oxidized $Fe^{\delta+}$ species within a mixed oxide matrix, aiming to preserve C−H bond selectivity. The resulting catalyst exhibited $Fe^{\delta+}$ species that were resistant to full reduction at reaction temperatures, achieving Fe-time yields between 2.0 and 5.6 $mmol_{C3H6} \cdot mol_{Fe}^{-1} \cdot s^{-1}$.

Time-resolved characterization techniques, including modulation-excitation, decoded two parallel pathways in which active Fe species participate in CO_2−PDH. A less-selective Mars − van Krevelen two-step pathway, involving ~ 1% of the total Fe content, features a reversible $Fe^{3+} \rightleftharpoons Fe^{3+/2+} \rightleftharpoons Fe^{2+}$ redox couple. This transforms a minority $MgFe_2O_4$-like surface

https://doi.org/10.1021/acscatal.5c09151
ACS Catal. 2026, 16, 3999−4016

phase to dispersed Fe^{2+} species. The latter Fe^{2+} species are allocated as the C−H bond selective site in a parallel, Langmuir − Hinshelwood pathway, which likely occurs through Lewis acid−base interactions between propane and $Fe^{2+} - O^{2-}$ pairs. While the exact nature of these selective Fe^{2+} species remains elusive, a distorted or asymmetric local environment is hypothesized based on the evidence presented in this work.

Catalyst deactivation occurs through irreversible $Fe^{3+} \rightleftharpoons Fe^{3+/2+} \rightleftharpoons Fe^{2+}$ transitions, in which aggregated, nonselective Fe^{2+} species are formed that contribute to carbon formation. These aggregated Fe^{2+} species are not fully reincorporated into the $MgFe_2O_4$-like surface phase upon CO_2 exposure, thereby depleting this minority spinel phase.

Comparing CO_2-assisted to regular PDH over the proposed catalyst $Mg(Fe,Al)O_x$, adding CO_2 induces competition between propane and CO_2 over the available active sites, thereby reducing the activity. A dualistic role of CO_2 then arises: by enabling the $Fe^{3+} \rightleftharpoons Fe^{3+/2+} \rightleftharpoons Fe^{2+}$ redox transition, CO_2 can assist in the removal of carbon, in the oxidation of H_2 via RWGS, and in suppressing FeO_x aggregation. By doing so, however, the formed Fe^{3+} species can overoxidize hydrocarbons. As for the highly selective, dispersed Fe^{2+} site, this can be transformed to Fe^{3+} upon oxidation by CO_2, ending up in the less selective Mars-Van Krevelen mechanism.

These findings highlight the power of dynamic characterization in revealing mechanistic phenomena that static techniques may overlook. As such, not only is the importance of $Fe^{\delta+}$ dispersion underscored, but the stabilization and relative speciation of Fe^{3+} vs Fe^{2+} also emerge as a catalyst design parameter. An improved balance between CO_2 activation and C−H bond activation can be achieved by tuning the reactor configuration and operating conditions, or by adjusting the material composition.

■ ASSOCIATED CONTENT

Supporting Information

The Supporting Information is available free of charge at https://pubs.acs.org/doi/10.1021/acscatal.5c09151.

> Performance of Fe-based catalysts for (CO_2-assisted) alkane dehydrogenation in the literature; depiction of in situ X-ray diffraction setup; synthesis protocol of reference $MgFe_2O_4$ and $Mg_2Fe_2O_5$ materials; N_2 physisorption isotherm of the as-prepared $Mg(Fe,Al)O_x$ catalyst; verification of mass and heat transfer limitations; in situ XRD with steady-state treatments and with ME H_2-CO_2 treatments; in situ QXAS with steady-state treatments; ab initio FDMNES simulations of the XANES region for reference FeO_x materials; EXAFS fitting results and structures used for fitting; details on H_2-TPR treatment; in situ QXAS with ME treatment; and schematic representation of deactivation behavior during CO_2−PDH (PDF)

■ AUTHOR INFORMATION

Corresponding Author

Vladimir V. Galvita − *Laboratory for Chemical Technology, Ghent University, B-9052 Ghent, Belgium;* orcid.org/0000-0001-9205-7917; Email: Vladimir.Galvita@UGent.be

Authors

Lennert A. D'ooghe − *Laboratory for Chemical Technology, Ghent University, B-9052 Ghent, Belgium;* orcid.org/0000-0002-3658-0540

Servaas Lips − *Laboratory for Chemical Technology, Ghent University, B-9052 Ghent, Belgium*

Soumya Kumar Das − *Laboratory for Chemical Technology, Ghent University, B-9052 Ghent, Belgium; ESRF, The European Synchrotron, 38043 Grenoble Cédex 9, France;* orcid.org/0009-0000-5382-4175

Lukas C. Buelens − *Laboratory for Chemical Technology, Ghent University, B-9052 Ghent, Belgium;* orcid.org/0000-0002-4896-1498

Alessandro Longo − *ESRF, The European Synchrotron, 38043 Grenoble Cédex 9, France; Istituto Studio dei Materiali Nanostrutturati-CNR, 90146 Palermo, Italy;* orcid.org/0000-0002-5381-7810

Hilde Poelman − *Laboratory for Chemical Technology, Ghent University, B-9052 Ghent, Belgium;* orcid.org/0000-0003-4267-7397

Kevin M. Van Geem − *Laboratory for Chemical Technology, Ghent University, B-9052 Ghent, Belgium;* orcid.org/0000-0003-4191-4960

Complete contact information is available at: https://pubs.acs.org/10.1021/acscatal.5c09151

Notes

The authors declare no competing financial interest.

■ ACKNOWLEDGMENTS

This work was supported by the European Research Council under the European Union's Horizon 2020 research and innovation program (ERC grant agreement n° 818607 and n° 101142065). We gratefully acknowledge the financial support of the Flemish Government and Flanders Innovation & Entrepreneurship (VLAIO) through the Moonshot project CAMELEON (HBC.2023.0551). L.C.B. acknowledges funding by the Fund for Scientific Research Flanders (FWO Flanders) through postdoctoral grant number 12E5623N. XRD experiments were performed at the "*ID20*" beamline at ESRF, Grenoble (proposal number CH7049). We are grateful to the staff of the ID20 beamline for their assistance during the measurements. QXAS experiments were performed on the "*ROCK*" beamline at SOLEIL Synchrotron, France, (proposal number 20240975). We are grateful to Dr. Anthony Beauvois for his assistance and to the SOLEIL staff for smoothly running the facility. STEM measurements were performed by L.C.B. at the UGent TEM Core Facility.

■ REFERENCES

(1) Amghizar, I.; Vandewalle, L. A.; Van Geem, K. M.; Marin, G. B. New Trends in Olefin Production. *Engineering* **2017**, *3* (2), 171−178.

(2) Rigamonti, M. G.; Shah, M.; Gambu, T. G.; Saeys, M.; Dusselier, M. Reshaping the Role of CO2 in Propane Dehydrogenation: From Waste Gas to Platform Chemical. *ACS Catal.* **2022**, *12* (15), 9339−9358.

(3) Monai, M.; Gambino, M.; Wannakao, S.; Weckhuysen, B. M. Propane to Olefins Tandem Catalysis: A Selective Route Towards Light Olefins Production. *Chem. Soc. Rev.* **2021**, *50* (20), 11503−11529.

(4) Sattler, J. J. H. B.; Ruiz-Martinez, J.; Santillan-Jimenez, E.; Weckhuysen, B. M. Catalytic Dehydrogenation of Light Alkanes on Metals and Metal Oxides. *Chem. Rev.* **2014**, *114* (20), 10613−10653.

(5) Eisele, P.; Killpack, R. Propene. *Ullmann's Encyclopedia of Industrial Chemistry*; Wiley, 2011.
(6) Bhasin, M. M.; McCain, J. H.; Vora, B. V.; Imai, T.; Pujadó, P. R. Dehydrogenation and Oxydehydrogenation of Paraffins to Olefins. *Appl. Catal. A Gen* **2001**, *221*, 397−419.
(7) Olbrich, M. E. Group VIII Catalyst Supported on Mixture of Zinc Aluminate and Calcium Aluminate. US5143888, September 1, 1992.
(8) Nawaz, Z. Light Alkane Dehydrogenation to Light Olefin Technologies: A Comprehensive Review. *Reviews in Chemical Engineering* **2015**, *31* (5), 413−436.
(9) Wang, G.; Zhu, X.; Li, C. Recent Progress in Commercial and Novel Catalysts for Catalytic Dehydrogenation of Light Alkanes. *Chem. Rec.* **2020**, *20* (6), 604−616.
(10) Atanga, M. A.; Rezaei, F.; Jawad, A.; Fitch, M.; Rownaghi, A. A. Oxidative Dehydrogenation of Propane to Propylene With Carbon Dioxide. *Appl. Catal., B* **2018**, *220*, 429−445.
(11) Gomez, E.; Yan, B.; Kattel, S.; Chen, J. G. Carbon Dioxide Reduction in Tandem With Light-Alkane Dehydrogenation. *Nat. Rev. Chem.* **2019**, *3* (11), 638−649.
(12) Carrero, C. A.; Schloegl, R.; Wachs, I. E.; Schomaecker, R. Critical Literature Review of the Kinetics for the Oxidative Dehydrogenation of Propane Over Well-Defined Supported Vanadium Oxide Catalysts. *ACS Catal.* **2014**, *4* (10), 3357−3380.
(13) Cavani, F.; Ballarini, N.; Cericola, A. Oxidative Dehydrogenation of Ethane and Propane: How Far From Commercial Implementation? *Catal. Today* **2007**, *127* (1−4), 113−131.
(14) Chauvy, R.; De Weireld, G. CO2 Utilization Technologies in Europe: A Short Review. *Energy Technology* **2020**, *8* (12), 2000627.
(15) Veeraraghavan Srinath, N.; Poelman, H.; Buelens, L.; Dendooven, J.; Reyniers, M.-F.; Marin, G. B.; Galvita, V. V. Behaviour of Platinum-Tin During CO2-Assisted Propane Dehydrogenation: Insights From Quick X-Ray Absorption Spectroscopy. *J. Catal.* **2022**, *408*, 356−371.
(16) D'ooghe, L. A.; Srinath, N. V.; De Coster, V.; Geerardyn, K. D. J.; Buelens, L. C.; Poelman, H.; Dendooven, J.; Reyniers, M.-F.; Van Geem, K. M.; Galvita, V. V. Detailing the Redox Ability of Supported Pt-Sn and Pt-In Catalysts for CO2-Assisted PDH. *J. Catal.* **2025**, *442*, No. 115855.
(17) D'ooghe, L. A.; Srinath, N. V.; De Coster, V.; Poelman, H.; Dendooven, J.; Reyniers, M. F.; Van Geem, K. M.; Galvita, V. V. Detailing the Activity and Deactivation of Supported Pt-Sn and Pt-In Catalysts for CO2-Assisted PDH. *J. Catal.* **2025**, *443*, 115943.
(18) Bathena, T.; Phung, T.; Murugesan, V.; Goulas, K. A.; Karakoti, A. S.; Ramasamy, K. Transition Metal Oxides in CO2 Driven Oxidative Dehydrogenation: Uncovering Their Redox Properties. *Journal of CO2 Utilization* **2024**, *84*, 102848.
(19) Van Cauwelaert, M. W. F.; Buelens, L. C.; Singh, V.; Poelman, H.; Detavernier, C.; Padevět, J.; Schwarzová, H.; Galvita, V. V.; Van Geem, K. M. Impact of Reduction Degree on Stability of Fe2O3-MgAl2O4 Oxygen Storage Materials During Chemical Looping Reverse Water-Gas Shift Reaction. *Journal of CO2 Utilization* **2024**, *88*, 102917.
(20) Loiland, J. A.; Wulfers, M. J.; Marinkovic, N. S.; Lobo, R. F. Fe/γ-Al2O3 and Fe-K/γ-Al2O3 as Reverse Water-Gas Shift Catalysts. *Catal. Sci. Technol.* **2016**, *6* (14), 5267−5279.
(21) Chou, C. Y.; Loiland, J. A.; Lobo, R. F. Reverse Water-Gas Shift Iron Catalyst Derived From Magnetite. *Catalysts* **2019**, *9* (9), 773.
(22) Wenzel, M.; Dharanipragada, A. N. V. R.; Galvita, V. V.; Poelman, H.; Marin, G. B.; Rihko-Struckmann, L.; Sundmacher, K. CO Production From CO2 via Reverse Water-Gas Shift Reaction Performed in a Chemical Looping Mode: Kinetics on Modified Iron Oxide. *Journal of CO2 Utilization* **2017**, *17*, 60−68.
(23) Panaritis, C.; Zgheib, J.; Ebrahim, S. A. H.; Couillard, M.; Baranova, E. A. Electrochemical In-Situ Activation of Fe-Oxide Nanowires for the Reverse Water Gas Shift Reaction. *Appl. Catal., B* **2020**, *269*, 118826.
(24) Daza, Y. A.; Kuhn, J. N. CO2 Conversion by Reverse Water Gas Shift Catalysis: Comparison of Catalysts, Mechanisms and Their Consequences for CO2 Conversion to Liquid Fuels. *RSC Adv.* **2016**, *6* (55), 49675−49691.
(25) Otroshchenko, T.; Jiang, G.; Kondratenko, V. A.; Rodemerck, U.; Kondratenko, E. V. Current Status and Perspectives in Oxidative, Non-Oxidative and CO2-Mediated Dehydrogenation of Propane and Isobutane Over Metal Oxide Catalysts. *Chem. Soc. Rev.* **2021**, *50* (1), 473−527.
(26) Sun, Y.-n.; Tao, L.; You, T.; Li, C.; Shan, H. Effect of Sulfation on the Performance of Fe2O3/Al2O3 Catalyst in Catalytic Dehydrogenation of Propane to Propylene. *Chemical Engineering Journal* **2014**, *244*, 145−151.
(27) Hu, B.; Schweitzer, N. M.; Zhang, G.; Kraft, S. J.; Childers, D. J.; Lanci, M. P.; Miller, J. T.; Hock, A. S. Isolated Fe II on Silica as a Selective Propane Dehydrogenation Catalyst. *ACS Catal.* **2015**, *5* (6), 3494−3503.
(28) Alghannam, A.; Bell, A. T. Effects of Cofeeding Hydrogen on Propane Dehydrogenation Catalyzed by Isolated Iron Sites Incorporated into Dealuminated BEA. *J. Am. Chem. Soc.* **2025**, *147* (2), 1677−1693.
(29) Tan, S.; Hu, B.; Kim, W. G.; Pang, S. H.; Moore, J. S.; Liu, Y.; Dixit, R. S.; Pendergast, J. G.; Sholl, D. S.; Nair, S.; Jones, C. W. Propane Dehydrogenation over Alumina-Supported Iron/Phosphorus Catalysts: Structural Evolution of Iron Species Leading to High Activity and Propylene Selectivity. *ACS Catal.* **2016**, *6* (9), 5673−5683.
(30) Torres Galvis, H. M.; Bitter, J. H.; Khare, C. B.; Ruitenbeek, M.; Dugulan, I. A.; de Jong, K. P. Supported Iron Nanoparticles as Catalysts for Sustainable Production of Lower Olefins. *Science (1979)* **2012**, *335* (6070), 835−838.
(31) Theofanidis, S. A.; Kasun Kalhara Gunasooriya, G. T.; Itskou, I.; Tasioula, M.; Lemonidou, A. A. On-Purpose Ethylene Production via CO2-Assisted Ethane Oxidative Dehydrogenation: Selectivity Control of Iron Oxide Catalysts. *ChemCatChem.* **2022**, *14* (14), e202200032.
(32) Michorczyk, P.; Kuśtrowski, P.; Chmielarz, L.; Ogonowski, J. Influence of Redox Properties on the Activity of Iron Oxide Catalysts in Dehydrogenation of Propane with CO2. *React. Kinet. Catal. Lett.* **2004**, *82* (1), 121−130.
(33) Wang, Y.; Chen, Y.; Zhang, J.; Ma, Q.; Fan, S.; Zhao, T. S. High Transformation of Propane in Reaction With CO2 to Propylene on ZrO2-Combined Fe-Based Catalysts. *Catal. Sci. Technol.* **2023**, *13* (19), 5734−5744.
(34) Wang, Y.; Wan, Z.; Ma, Q.; Zhang, J.; Fan, S.; Gao, X.; Zhao, T. S. Co-Modified Fe2O3-ZrO2 for Catalyzing Propane and CO2 Reaction to Propylene. *New J. Chem.* **2024**, *48* (23), 10607−10615.
(35) Jeong, M. H.; Sun, J.; Young Han, G.; Lee, D. H.; Bae, J. W. Successive Reduction-Oxidation Activity of FeOx/TiO2 for Dehydrogenation of Ethane and Subsequent CO2 Activation. *Appl. Catal., B* **2020**, *270*, 118887−118901.
(36) Li, G.; Liu, C.; Cui, X.; Yang, Y.; Shi, F. Oxidative Dehydrogenation of Light Alkanes with Carbon Dioxide. *Green Chem.* **2021**, *23* (2), 689−707.
(37) Bennett, C. O. A Dynamic Method for the Study of Heterogeneous Catalytic Kinetics. *AIChE J.* **1967**, *13* (5), 890−895.
(38) Müller, P.; Hermans, I. Applications of Modulation Excitation Spectroscopy in Heterogeneous Catalysis. *Ind. Eng. Chem. Res.* **2017**, *56* (5), 1123−1136.
(39) Yang, Q.; Fedorova, E. A.; Cao, D. B.; Saraçi, E.; Kondratenko, V. A.; Kreyenschulte, C. R.; Lund, H.; Bartling, S.; Weiß, J.; Doronkin, D. E.; Grunwaldt, J. D.; Brückner, A.; Jiao, H.; Kondratenko, E. V. Understanding Mn-Modulated Restructuring of Fe-Based Catalysts for Controlling Selectivity in CO2 Hydrogenation to Olefins. *Nat. Catal* **2025**, *8*, 595.
(40) Wan, G.; Zhang, G.; Chen, J. Z.; Toney, M. F.; Miller, J. T.; Tassone, C. J. Reaction-Mediated Transformation of Working Catalysts. *ACS Catal.* **2022**, *12* (13), 8007−8018.
(41) de Roy, A.; Forano, C.; Besse, J. P. Layered Double Hydroxides: Synthesis and Post-Synthesis Modification. In *Layered*

https://doi.org/10.1021/acscatal.5c09151
ACS Catal. 2026, 16, 3999−4016

Double Hydroxides: Present and Future; Rives, V., Ed.; Nova Science Publishers, Inc.: New York, 2006; pp 1−39.
(42) Liu, G.; Yang, J.; Xu, X. Synthesis of Hydrotalcite-Type Mixed Oxide Catalysts From Waste Steel Slag for Transesterification of Glycerol and Dimethyl Carbonate. *Sci. Rep* **2020**, *10* (1), 10273.
(43) Kumar Das, S.; D'ooghe, L.; Srinath, N. V.; Theofanidis, S. A.; Longo, A.; Sahle, C.; Van Geem, K.; Poelman, H.; Poelman, D.; Galvita, V. Evolution of Low Z-Elements in a Ni/MgFeAlO4 Catalyst during Reaction: Insight from In Situ XRS. *ACS Catal.* **2024**, *14* (3), 1311−1323.
(44) De Coster, V.; Srinath, N. V.; Yazdani, P.; Poelman, H.; Galvita, V. V. Dual-Element Modulation Excitation XAS to Probe the Redox Surface Chemistry of a Ni-Fe Dry Reforming Catalyst. *ACS Catal.* **2023**, *13* (19), 12445−12457.
(45) Theofanidis, S. A.; Loizidis, C.; Heracleous, E.; Lemonidou, A. A. CO2-Oxidative Ethane Dehydrogenation Over Highly Efficient Carbon-Resistant Fe-Catalysts. *J. Catal.* **2020**, *388*, 52−65.
(46) Tasioula, M.; de Clermont Gallerande, E.; Theofanidis, S. A.; Longo, A.; Lomachenko, K. A.; Sahle, C.; Lemonidou, A. A. Tandem CO2 Valorization and Ethane Dehydrogenation: Elucidating the Nature of Highly Selective Iron Oxide Active Sites. *ACS Catal.* **2023**, *13* (4), 2176−2189.
(47) Rampelberg, G.; De Schutter, B.; Devulder, W.; Martens, K.; Radu, I.; Detavernier, C. In Situ X-Ray Diffraction Study of the Controlled Oxidation and Reduction in the V-O System for the Synthesis of VO2 and V2O3 Thin Films. *J. Mater. Chem. C Mater.* **2015**, *3* (43), 11357−11365.
(48) Baurecht, D.; Porth, I.; Fringeli, U. P. A New Method of Phase Sensitive Detection in Modulation Spectroscopy Applied to Temperature Induced Folding and Unfolding of RNase A. *Vib Spectrosc* **2002**, *30* (1), 85−92.
(49) Urakawa, A.; Bürgi, T.; Baiker, A. Sensitivity Enhancement and Dynamic Behavior Analysis by Modulation Excitation Spectroscopy: Principle and Application in Heterogeneous Catalysis. *Chem. Eng. Sci.* **2008**, *63* (20), 4902−4909.
(50) Marchionni, V.; Ferri, D.; Kröcher, O.; Wokaun, A. Increasing the Sensitivity to Short-Lived Species in a Modulated Excitation Experiment. *Anal. Chem.* **2017**, *89* (11), 5801−5809.
(51) Ferri, D.; Newton, M. A.; Nachtegaal, M. Modulation Excitation X-Ray Absorption Spectroscopy to Probe Surface Species on Heterogeneous Catalysts. *Top Catal* **2011**, *54* (16−18), 1070−1078.
(52) Routh, P. K.; Redekop, E.; Prodinger, S.; van der Hoeven, J. E. S.; Lim, K. R. G.; Aizenberg, J.; Nachtegaal, M.; Clark, A. H.; Frenkel, A. I. Restructuring Dynamics of Surface Species in Bimetallic Nanoparticles Probed by Modulation Excitation Spectroscopy. *Nat. Commun.* **2024**, *15* (1), 6736.
(53) Huotari, S.; Sahle, C. J.; Henriquet, C.; Al-Zein, A.; Martel, K.; Simonelli, L.; Verbeni, R.; Gonzalez, H.; Lagier, M. C.; Ponchut, C.; Moretti Sala, M.; Krisch, M.; Monaco, G. A Large-Solid-Angle X-Ray Raman Scattering Spectrometer at ID20 of the European Synchrotron Radiation Facility. *J. Synchrotron Radiat* **2017**, *24* (2), 521−530.
(54) Sahle, C. J.; Majkut, M.; Ruotsalainen, K. O.; Gerbon, F.; Suomalainen, N.; Lagier, M. C.; Detlefs, B.; Claustre, L.; Mirone, A.; Longo, A. A Miniature X-Ray Diffraction Setup on ID20 at the European Synchrotron Radiation Facility. *J. Synchrotron Radiat* **2024**, *31*, 1622−1626.
(55) La Fontaine, C.; Belin, S.; Barthe, L.; Roudenko, O.; Briois, V. ROCK: A Beamline Tailored for Catalysis and Energy-Related Materials from Ms Time Resolution to Mm Spatial Resolution. *Synchrotron Radiat News* **2020**, *33* (1), 20−25.
(56) Briois, V.; La Fontaine, C.; Belin, S.; Barthe, L.; Moreno, T.; Pinty, V.; Carcy, A.; Girardot, R.; Fonda, E. ROCK: The New Quick-EXAFS Beamline at SOLEIL. *J. Phys. Conf Ser.* **2016**, *712* (1), No. 012149.
(57) De Coster, V. *Structural Dynamics of Nanoalloys in Catalytic Reaction: A Modulated Approach*; Ghent University: Ghent, 2023.
(58) De Coster, V.; Srinath, N. V.; Yazdani, P.; Poelman, H.; Galvita, V. V. Modulation Engineering: Stimulation Design for Enhanced Kinetic Information from Modulation-Excitation Experiments on Catalytic Systems. *ACS Catal.* **2023**, *13* (7), 5084−5095.
(59) Newville, M. Larch: An Analysis Package for XAFS and Related Spectroscopies. *J. Phys.: Conf. Ser.* **2013**, *430*, 012007.
(60) Boubnov, A.; Lichtenberg, H.; Mangold, S.; Grunwaldt, J. D. Identification of the Iron Oxidation State and Coordination Geometry in Iron Oxide- and Zeolite-Based Catalysts Using Pre-Edge XAS Analysis. *J. Synchrotron Radiat* **2015**, *22* (2), 410−426.
(61) Stern, E. A. Number of Relevant Independent Points in X-Ray-Absorption Fine-Structure Spectra. *Phys. Rev. B* **1993**, *48* (13), 9825−9827.
(62) De Coster, V.; Poelman, H.; Galvita, V. V. *ME(XAS)-PSD Analysis Toolbox*. Zenodo: Ghent, January 27, 2023.
(63) Jaumot, J.; Gargallo, R.; De Juan, A.; Tauler, R. A Graphical User-Friendly Interface for MCR-ALS: A New Tool for Multivariate Curve Resolution in MATLAB. *Chemometrics and Intelligent Laboratory Systems* **2005**, *76* (1), 101−110.
(64) Jaumot, J.; de Juan, A.; Tauler, R. MCR-ALS GUI 2.0: New Features and Applications. *Chemometrics and Intelligent Laboratory Systems* **2015**, *140*, 1−12.
(65) Carberry, J. J. *Chemical and Catalytic Reaction Engineering*; Dover Publications, Inc.: New York, 2001.
(66) Froment, G. F.; Bischoff, K. B.; De Wilde, J. *Chemical Reactor Analysis and Design*, 3rd ed.; John Wiley & Sons, Inc., 2011.
(67) Mears, D. E. Diagnostic Criteria for Heat Transport Limitations in Fixed Bed Reactors. *J. Catal.* **1971**, *20* (2), 127−131.
(68) Finlayson, B. A. *Introduction to Chemical Engineering Computing*, 2nd ed.; John Wiley & Sons, Inc.: Hoboken, NJ, 2012.
(69) Thommes, M.; Kaneko, K.; Neimark, A. V.; Olivier, J. P.; Rodriguez-Reinoso, F.; Rouquerol, J.; Sing, K. S. W. Physisorption of Gases, with Special Reference to the Evaluation of Surface Area and Pore Size Distribution (IUPAC Technical Report). *Pure Appl. Chem.* **2015**, *87* (9−10), 1051−1069.
(70) Bellotto, M.; Rebours, B.; Clause, O.; Lynch, J.; Bazin, D.; Elkaïm, E. A Reexamination of Hydrotalcite Crystal Chemistry. *J. Phys. Chem.* **1996**, *100* (20), 8527−8534.
(71) Cavani, F.; Trifirò, F.; Vaccari, A. Hydrotalcite-Type Anionic Clays: Preparation, Properties and Applications. *Catal. Today* **1991**, *11* (2), 173−301.
(72) Filez, M.; Redekop, E. A.; Poelman, H.; Galvita, V. V.; Meledina, M.; Turner, S.; Van Tendeloo, G.; Detavernier, C.; Marin, G. B. One-Pot Synthesis of Pt Catalysts Based on Layered Double Hydroxides: An Application in Propane Dehydrogenation. *Catal. Sci. Technol.* **2016**, *6* (6), 1863−1869.
(73) Bellotto, M.; Rebours, B.; Clause, O.; Lynch, J.; Bazin, D.; Elka1, E. Hydrotalcite Decomposition Mechanism: A Clue to the Structure and Reactivity of Spinel-like Mixed Oxides. *J. Phys. Chem.* **1996**, *100* (20), 8535−8542.
(74) Yan, B.; Yao, S.; Kattel, S.; Wu, Q.; Xie, Z.; Gomez, E.; Liu, P.; Su, D.; Chen, J. G. Active Sites for Tandem Reactions of CO2 Reduction and Ethane Dehydrogenation. *Proc. Natl. Acad. Sci. U. S. A.* **2018**, *115* (33), 8278−8283.
(75) Du, Q.; Zhang, X.; Wang, F.; Liu, W. Oxidative Dehydrogenation of Ethane to Ethylene With CO2 via Mg-Al Spinel Catalysts: Insight Into Dehydrogenation Mechanism. *Carbon Capture Science and Technology* **2025**, *14*, 100327.
(76) Chernyshov, D.; Van Beek, W.; Emerich, H.; Milanesio, M.; Urakawa, A.; Viterbo, D.; Palin, L.; Caliandro, R. Kinematic Diffraction on a Structure With Periodically Varying Scattering Function. *Acta Crystallogr. A* **2011**, *67* (4), 327−335.
(77) Jiang, L. *Phase Sensitive Detected X-Ray Absorption Spectroscopy to Study Real Industrial Oxidation Catalyst*; Université de Lille: Lille, France, 2024.
(78) Westre, T. E.; Kennepohl, P.; Dewitt, J. G.; Hedman, B.; Hodgson, K. O.; Solomon, E. I. A Multiplet Analysis of Fe K-Edge 1→3d Pre-Edge Features of Iron Complexes. *J. Am. Chem. Soc.* **1997**, *119* (27), 6297−6314.

https://doi.org/10.1021/acscatal.5c09151
ACS Catal. 2026, 16, 3999−4016

(79) Hilbrandt, N.; Martin, M. A Quantitative In Situ Fe K-XAFS Study (T > 1270 K) on the Oxidation Degree of Iron in (Mg1-XFex)1-ΔO. *J. Synchrotron Radiat* **1999**, *6*, 489−491.
(80) Kuzmin, A.; Mironova, N.; Purans, J.; Sazonov, A. EXAFS and XANES Studies of CoxMg1-XO Solid Solutions Using a Laboratory EXAFS Spectrometer. *Physica Status Solidi (a)* **1993**, *135* (1), 133−141.
(81) Wilke, M.; Farges, F.; Petit, P.-E.; Brown, G. E., Jr.; Martin, F. Oxidation State and Coordination of Fe in Minerals - An Fe K-XANES Spectroscopic Study. *Am. Mineral.* **2001**, *86*, 714−730.
(82) Niedermaier, M.; Schwab, T.; Dolcet, P.; Bernardi, J.; Gross, S.; Bockstedte, M.; Diwald, O. Cobalt and Iron Ions in MgO Nanocrystals: Should They Stay or Should They Go. *J. Phys. Chem. C* **2019**, *123* (42), 25991−26004.
(83) De Coster, V.; Srinath, N. V.; Yazdani, P.; Poelman, H.; Galvita, V. V. Dual-Element Modulation Excitation XAS to Probe the Redox Surface Chemistry of a Ni-Fe Dry Reforming Catalyst. *ACS Catal.* **2023**, *13* (19), 12445−12457.
(84) Zhu, J.; Zeng, Z.; Li, W. X. K-Edge XANES Investigation of Fe-Based Oxides by Density Functional Theory Calculations. *J. Phys. Chem. C* **2021**, *125* (47), 26229−26239.
(85) Shannon, R. D. Revised Effective Ionic Radii and Systematic Studies of Interatomie Distances in Halides and Chaleogenides. *Acta Crystallogr., Sect. A* **1976**, *32* (5), 751−767.
(86) Srinivasan, P. D.; Patil, B. S.; Zhu, H.; Bravo-Suárez, J. J. Application of Modulation Excitation-Phase Sensitive Detection-DRIFTS for In Situ /Operando Characterization of Heterogeneous Catalysts. *React. Chem. Eng.* **2019**, *4* (5), 862−883.
(87) Marchionni, V.; Newton, M. A.; Kambolis, A.; Matam, S. K.; Weidenkaff, A.; Ferri, D. A Modulated Excitation ED-EXAFS/DRIFTS Study of Hydrothermal Ageing of Rh/Al2O3. *Catal. Today* **2014**, *229*, 80−87.
(88) Chang, Q.; Li, K.; Zhang, C.; Cheruvathur, A. V.; Zheng, L.; Yang, Y.; Li, Y. XAFS Studies of Fe−SiO2 Fischer−Tropsch Catalyst During Activation in CO, H2, and Synthesis Gas. *ChemCatChem.* **2019**, *11* (8), 2206−2216.
(89) Longo, A.; Theofanidis, S. A.; Cavallari, C.; Srinath, N. V.; Hu, J.; Poelman, H.; Sabbe, M. K.; Sahle, C. J.; Marin, G. B.; Galvita, V. V. What Makes Fe-Modified MgAl2O4 an Active Catalyst Support? Insight from X-Ray Raman Scattering. *ACS Catal.* **2020**, *10* (12), 6613−6622.
(90) Ferri, D.; Newton, M. A.; Di Michiel, M.; Chiarello, G. L.; Yoon, S.; Lu, Y.; Andrieux, J. Revealing the Dynamic Structure of Complex Solid Catalysts Using Modulated Excitation X-Ray Diffraction. *Angew. Chem.* **2014**, *126* (34), 9036−9040.
(91) Mohammadzadeh, H.; Shariati, A.; Khosravi-Nikou, M.; Zahedinejad, A. Improved Activity and Coking-Resistance of Fe2O3/ZrO2 Catalysts by Hydrothermal Synthesis in Propane Dehydrogenation With CO2: Experimental, DFT Calculations, and Deactivation Modeling. *J. Environ. Chem. Eng.* **2025**, *13* (1), 115002.
(92) Tanasoi, S.; Mitran, G.; Tanchoux, N.; Cacciaguerra, T.; Fajula, F.; Sndulescu, I.; Tichit, D.; Marcu, I. C. Transition Metal-Containing Mixed Oxides Catalysts Derived From LDH Precursors for Short-Chain Hydrocarbons Oxidation. *Appl. Catal. A Gen* **2011**, *395* (1−2), 78−86.
(93) Zhang, Y.; Qi, L.; Nozik, D.; Dun, C.; Urban, J. J.; Bell, A. T. Mechanism and Kinetics of Propane and N-Butane Dehydrogenation over Isolated and Nested ≡SiOZn-OH Sites Grafted onto Silanol Nests of Dealuminated Beta Zeolite. *ACS Catal.* **2024**, *14* (4), 2787−2804.
(94) Heredia, A. C.; Oliva, M. I.; Agú, U.; Zandalazini, C. I.; Marchetti, S. G.; Herrero, E. R.; Crivello, M. E. Synthesis, Characterization and Magnetic Behavior of Mg-Fe-Al Mixed Oxides Based on Layered Double Hydroxide. *J. Magn Magn Mater.* **2013**, *342*, 38−46.
(95) Tasioula, M.; Theofanidis, S. A.; de Clermont Gallerande, E.; Christodoulou, A.; Antzaras, A. N.; Delikonstantis, E.; Sahle, C. J.; Longo, A.; Lemonidou, A. A. CO2 Utilization and On-Purpose Ethylene Production: A Chemical Looping Approach. *Appl. Catal., B* **2025**, *362*, 124757.

https://doi.org/10.1021/acscatal.5c09151
ACS Catal. 2026, 16, 3999−4016